



저작자표시-비영리-변경금지 2.0 대한민국

이용자는 아래의 조건을 따르는 경우에 한하여 자유롭게

- 이 저작물을 복제, 배포, 전송, 전시, 공연 및 방송할 수 있습니다.

다음과 같은 조건을 따라야 합니다:



저작자표시. 귀하는 원저작자를 표시하여야 합니다.



비영리. 귀하는 이 저작물을 영리 목적으로 이용할 수 없습니다.



변경금지. 귀하는 이 저작물을 개작, 변형 또는 가공할 수 없습니다.

- 귀하는, 이 저작물의 재이용이나 배포의 경우, 이 저작물에 적용된 이용허락조건을 명확하게 나타내어야 합니다.
- 저작권자로부터 별도의 허가를 받으면 이러한 조건들은 적용되지 않습니다.

저작권법에 따른 이용자의 권리는 위의 내용에 의하여 영향을 받지 않습니다.

이것은 [이용허락규약\(Legal Code\)](#)을 이해하기 쉽게 요약한 것입니다.

[Disclaimer](#)

Thesis for the Degree of Master of Engineering

**Enhancement and optimization of the
printability of biomaterials for
extrusion-based bioprinting**



by

Myoung Hwan Kim

Interdisciplinary Program of Biomedical Mechanical & Electrical
Engineering

The Graduate School

Pukyong National University

August 2019

Enhancement and optimization of the printability of biomaterials for extrusion-based bioprinting

압출기반 바이오프린팅을 이용한
생체재료의 프린팅
개선 및 최적화 연구

Advisor: Prof. Seung Yun Nam

by

Myoung Hwan Kim

A thesis submitted in partial fulfillment of the requirements for the degree of
Master of Engineering

in Interdisciplinary Program of Biomedical Mechanical & Electrical
Engineering

The Graduate School

Pukyong National University

August 2019

**Enhancement and optimization of the printability of
biomaterials for extrusion-based bioprinting**

A dissertation

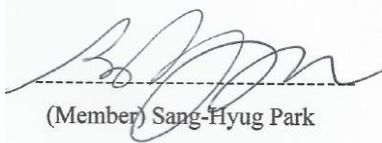
by

Myoung Hwan Kim

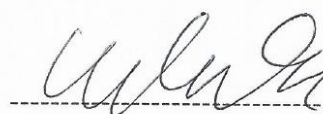
Approved by:



(Chairman) Won-Kyo Jung



(Member) Sang-Hyug Park



(Member) Seung Yun Nam

August 23, 2019

**Enhancement and optimization of the printability of biomaterials for extrusion-based
bioprinting**

Myoung Hwan Kim

Interdisciplinary Program of Biomedical Mechanical & Electrical Engineering

The Graduate School

Pukyong National University

Abstract

바이오프린팅은 다양한 생체재료를 이용하여 단시간 내에 높은 세포생존도를 가지는 세포지지체를 제작할 수 있어 최근 조직 공학 및 재생 의학 분야에서 각광받고 있다. 그러나 생체재료들의 각기 다른 기계적 특성 때문에 최적화된 프린팅 조건을 파악하기 어려워 정밀한 삼차원적 구조를 프린팅하기에는 상당히 제한적이다. 이를 해결하기 위하여 생체재료의 유변학적 및 기계적 특성들을 정확하게 분석하는 것이 중요하다. 따라서, 본 연구에서는 다양한 생체재료의 물성들을 정량적으로 분석하여 얻은 최적의 프린팅 조건으로 골조직 재생뿐만 아니라 연조직 재생을 위한 세포지지체를 압출기반 바이오프린팅으로 제작하였다. 이를 통해, 우수한 기계적 특성을 가지는 바이오프린팅용 생체재료를 이용하여 정밀하게 제작된 삼차원적 구조의 세포지지체를 기계적, 화학적 그리고 생물학적으로 평가하였다. 따라서 본 연구를 통해, 새로운 생체재료와 최적화된 바이오프린팅으로 뛰어난 세포지지체를 제작할 수 있는 방법을 제시하였다.

Table of contents

Abstract	i
Table of contents	ii
List of figures	v
1. Introduction	1
2. Characterization of the role of nano-hydroxyapatite (nHA) on 3D-printed PCL/nHA composite scaffolds	10
2.1. Materials and methods	12
2.1.1. Scaffold fabrication	12
2.1.2. Physicochemical characterization	12
2.1.3. Biological activities in PCL/nHA composite scaffolds	13
2.2. Results and discussion	14
2.2.1. Physical and chemical properties of PCL/nHA scaffolds	14
2.2.2. Morphological characterization and printability	17
2.2.3. Cell-scaffold interaction	19
2.3. Conclusion	21
3. Enhanced 3D printability of alginate-based hydrogels with carrageenan	22

3.1. Materials and methods	25
3.1.1. Hydrogel preparation	25
3.1.2. Rheological evaluation	25
3.1.3. Printability simulation and assessment	26
3.1.4. Bioprinting	28
3.1.5. Evaluation of 3D deposition fidelity	28
3.1.6. Bioprinting of Alg-Carr-CaSO₄ with stem cells	28
3.1.7. Cell viability	29
3.2. Results and discussion	31
3.2.1. Rheological characterization of Alg-CaSO₄	31
3.2.2. The effects of carrageenan on rheological characteristics of Alg-CaSO₄ hydrogel	33
3.2.3. Printability of Alg-CaSO₄ hydrogel	38
3.2.4. The effects of carrageenan on the printability of Alg-CaSO₄ hydrogel	42
3.2.5. Assessment of 3D deposition of Alg-CaSO₄ and Alg-Carr-CaSO₄ composite hydrogel	45
3.2.6. Biocompatibility of bioprinted scaffolds	47

3.3. Discussion	49
3.4. Conclusion	53
4. Conclusions	54
5. References	55
Acknowledgments	58



List of figure

Figure 1. Schematics of bioprinting for tissue engineering and regenerative medicine -----	4
Figure 2. Types of 3D bioprinting -----	5
Figure 3. Custom-made Microextrusion-based 3D bioprinter and its specification -----	6
Figure 4. Correlations of factors for 3D bioprinting -----	7
Figure 5. Characteristics of advanced bioinks -----	8
Figure 6. Properties of Newtonian and non-Newtonian bioinks in the syringe with dispensing pressure -----	9
Figure 7. Physicochemical characteristics: (a) FT-IR spectra; (b) Young's moduli of PCL/nHA composite scaffolds with different concentrations of nHA (n=3) -----	16
Figure 8. SEM images of the top, side, and surface views of the PCL/nHA composite scaffolds: (a) 0% nHA; (b) 10% nHA; (c) 20% nHA; (d) 30% nHA; (e) Strut diameter and pore size of the composite scaffolds -----	18
Figure 9. Biological activities on PCL/nHA composite scaffolds: (a) Cell proliferation with alamarBlue reagent; (b) Mineralization on the PCL/nHA	

composite scaffolds; (c) Atomic percentage of chemical elements in the PCL/nHA composite scaffolds ----- 20

Figure 10. Rheological assessment of Alg crosslinked with CaSO₄: (a) Shear moduli of Alg-CaSO₄; (b) Storage moduli at an angular frequency of 1 rad/s with different concentrations of CaSO₄ ----- 32

Figure 11. Flow curves of the shear rate sweep test of the Alg-Carr-CaSO₄ as a function of shear rate (0.01-1000 s⁻¹) ----- 35

Figure 12. Rheological assessment of Alg-Carr-CaSO₄: (a) Frequency sweep test of the Alg-Carr-CaSO₄ (0.1-500 rad/s); (b) Storage modulus at 1 rad/s angular frequency ----- 36

Figure 13. The recovery behaviors of the Alg-Carr-CaSO₄ at different shear rates (1 and 3: 0.1 s⁻¹ for 60 seconds, 2: 100 s⁻¹ for 10 seconds) ----- 37

Figure 14. Printability simulation and measurement of Alg-CaSO₄: (a) Microscopic images of printed struts at different printing parameters; (b) Printability simulation of Alg-CaSO₄ ----- 40

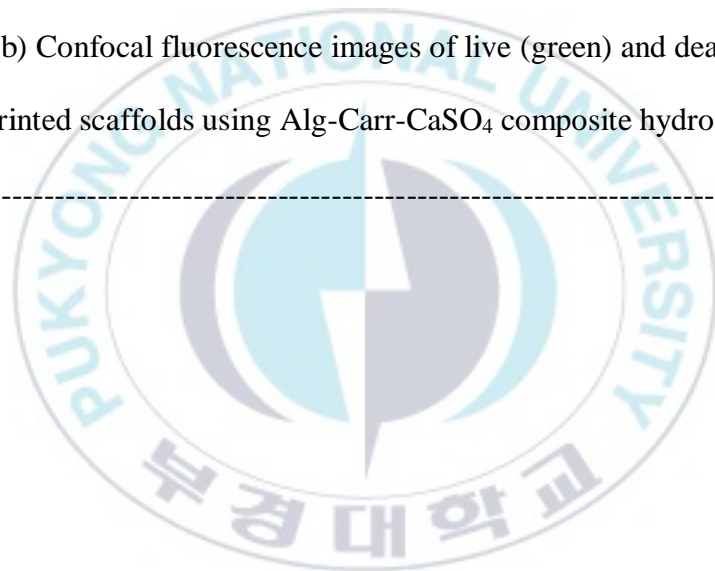
Figure 15. Strut diameter of printed Alg-CaSO₄: (a) Printed strut diameter (mm) represented as the average ± standard deviation (n = 10); (b) 3D diagram of printed strut diameter averages ----- 41

Figure 16. Printability simulation and measurement of Alg-Carr-CaSO₄: (a) Microscopic images of printed struts at different printing parameters; (b) Printability simulation of Alg-Carr-CaSO₄ ----- 43

Figure 17. Strut diameter of printed Alg-Carr-CaSO₄: (a) Printed strut diameter (mm) represented as the average ± standard deviation (n = 10); (b) 3D diagram of printed strut diameter averages ----- 44

Figure 18. Assessment of 3D deposition: (a and c) Top and side views of 3D deposition of Alg-CaSO₄; (b and d) Alg-Carr-CaSO₄ (Scale bar: 5 mm) ----- 46

Figure 19. Biological activities of 3D-bioprinted scaffolds: (a) Cell proliferation with alamarBlue reagent in Alg-CaSO₄ and Alg-Carr-CaSO₄ scaffolds; (b) Confocal fluorescence images of live (green) and dead (red) cells in 3D-bioprinted scaffolds using Alg-Carr-CaSO₄ composite hydrogels after 24 hours ----- 48



1. Introduction

Additive manufacturing techniques for fabricating 3D constructs with high efficacy in tissue regeneration have emerged in the field of tissue engineering and regenerative medicine [1]. The 3D constructs play significant roles in tissue engineering as they provide a framework for initial support to living cells and other functional components of extracellular matrix (ECM) [2]. Thus, the ECM assists in overall cell behaviors such as cell attachment, migration, proliferation, and maintaining the differential potential of the cells. Also, cell nutrients, byproducts, and biochemical factors can be transported through interconnected pore networks in the scaffold [3]. Thus, various prerequisites related to structural, mechanical and biological properties for successfully fabricating ECM-mimicked 3D scaffolds should be fulfilled e.g. porosity, pore size, interconnectivity, biological interaction, non-toxic, and non-inflammatory. However, conventional scaffold fabrication methods e.g. solvent casting, freeze drying, gas forming, electrospinning, and salt-leaching have critical limitations such as uncontrollable geometric features and a narrow range of selection of biomaterials [4]. To overcome these limitations, the 3D bioprinting technique has been proposed for complex tissue substitutes with precise positioning of biomaterials, biomolecules, and cells in the desired 3D structures [5] (Figure 1).

The types for 3D bioprinting are classified into inkjet-based bioprinting, laser-assisted bioprinting, and extrusion-based bioprinting according to the source of the

printing methods [6] (Figure 2). Among these printing types, extrusion-based bioprinting is the most commonly used because of the highest capability of printing using a wide range of biomaterials as well as for cell printing without significant negative effects on cell viability and convenient operating [7]. Also, heterogeneous 3D constructs using two or more different materials encapsulated with various types of cells could be fabricated for various applications.

Extrusion-based bioprinting is composed of a motion stage (x, y, and z), temperature controllers, and pneumatic controllers or motion axis for piston-driven type. Biomaterials are loaded into a syringe attached to the axes and extruded by mechanical forces or pressures according to the pre-designed paths through a needle. For the successful fabrication of 3D constructs using extrusion-based bioprinting, evaluation of the 3D printability based on the overall rheological properties of biomaterials, structural characteristics, and mathematical modeling is necessary (Figure 4). The rheological properties of the hydrogel play an important role in controlling the resolution and shape fidelity of the 3D-bioprinted structures [8, 9] (Figure 5). Also, the biomaterials with shear thinning properties have been most widely used in extrusion-based bioprinting because randomly arranged polymer chains of the biomaterials can be aligned and become extrudable by applying shear forces in the nozzle [10] (Figure 6). Based on rheological characteristics of the biomaterials including shear thinning and thixotropic behaviors, printing parameters calculated from mathematical modeling such as printing speed, pressure, and nozzle size can be optimized [11].

Due to the wide versatility of extrusion-based bioprinting among several other types of bioprinting, this thesis focuses on the applications with optimal printing parameters through evaluation of printability based on rheological properties of biomaterials. In this thesis, the custom-made extrusion-based bioprinting system (Microextrusion-based 3D bioprinter) was developed for various applications such as soft tissue, hard tissue, coaxial printing, and printing with photo-crosslinkable materials using a UV source (Figure 3). Microextrusion-based 3D bioprinter is composed of a motion stage driven by five servo motors, independent modular multi-printing head with two axes equipped with pistons, pneumatic controllers (<700 kPa), temperature controllers (<200°C), and real-time camera. There are two main projects using Microextrusion-based 3D bioprinter. Firstly, in Chapter 2, the role of hydroxyapatite, a known biocompatible biomaterial with excellent osteoconductive properties, was quantitatively monitored for its morphological, physical and biochemical characteristics in 3D-printed scaffolds for bone tissue engineering. Secondly, the optimization of printability, shape fidelity and 3D deposition based on the rheological properties of biomaterials was presented in Chapter 3. The experimental results demonstrated a methodological solution for improving the printability and shape fidelity of 3D constructs using 3D bioprinting for various applications in tissue engineering and regenerative medicine.

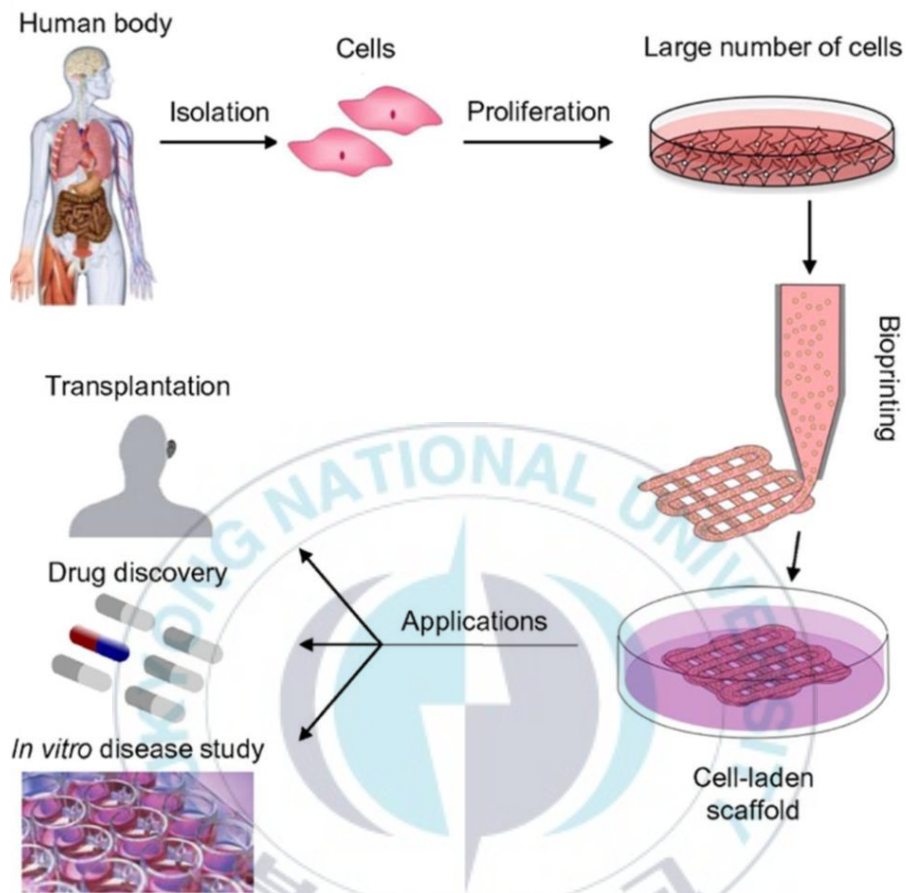
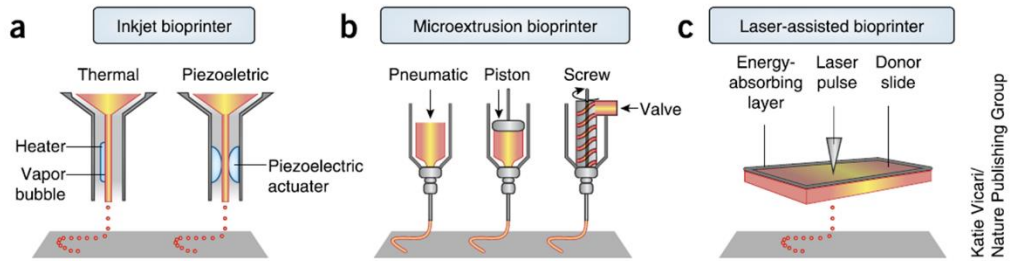


[Figure adapted from Nishat Tasnim (2018). "3D Bioprinting Stem Cell Derived Tissues".

Cellular and molecular bioengineering, 11(4), 219-240.]

Figure 1. Schematics of bioprinting for tissue engineering and regenerative medicine.



Katie V/cari/
Nature Publishing Group

[Figure adapted from Sean V Murphy and Anthony Atala (2014). “3D bioprinting of tissues and organs”. Nature biotechnology, 32(8), 773.]

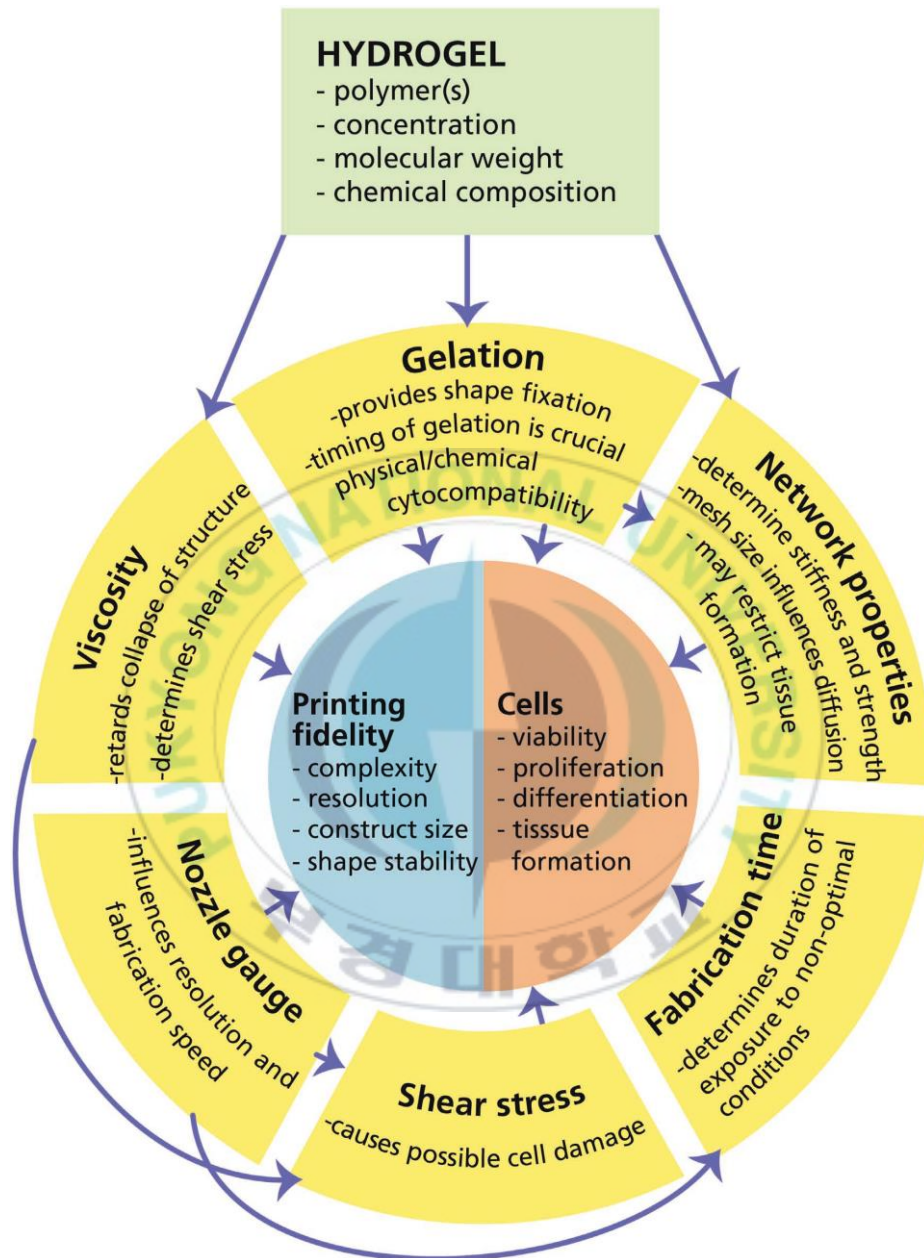
Figure 2. Types of 3D bioprinting.





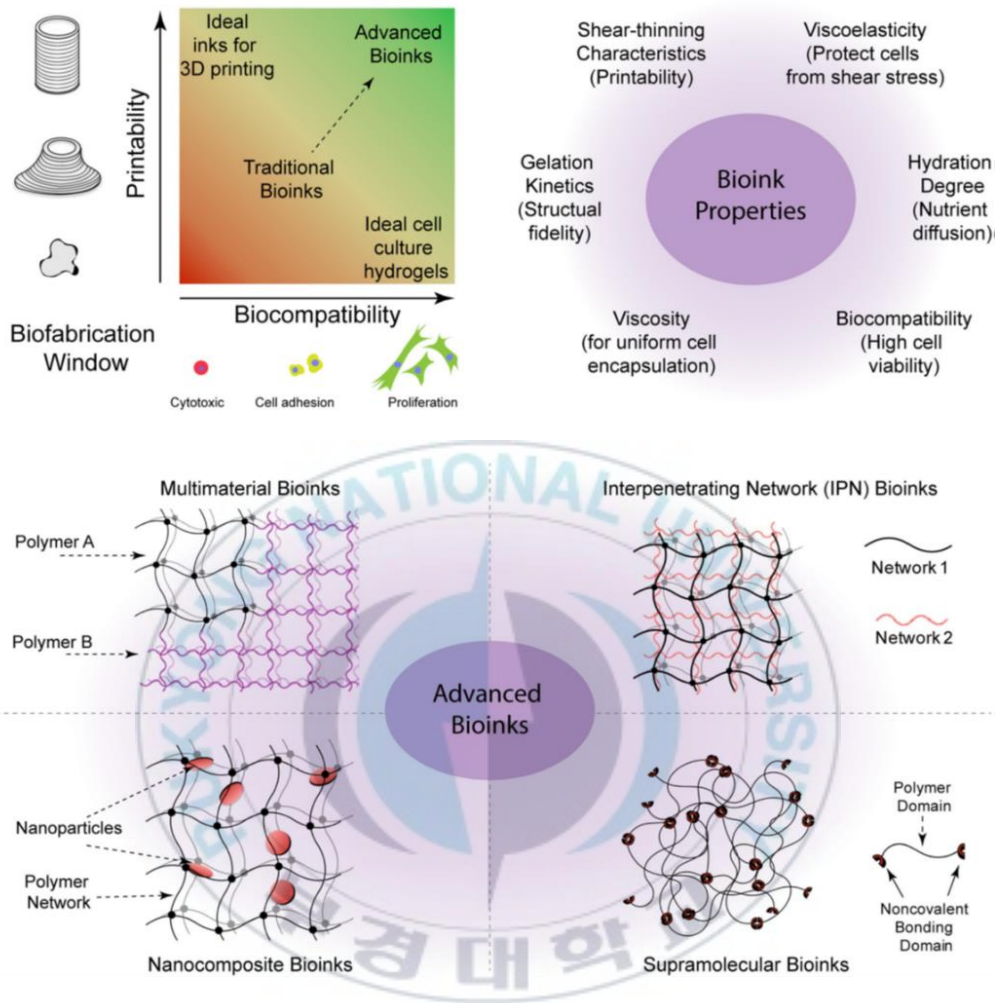
Working range (mm × mm × mm)	1300 × 1000 × 720	Resolution (mm)	0.01
Maximum speed (mm/s)	200	Temperature set range (°C)	< 200
Accuracy (mm)	0.03	Operating air pressure (kPa)	< 700
Repeatability (mm)	±0.005		

Figure 3. Custom-made Microextrusion-based 3D bioprinter and its specification.



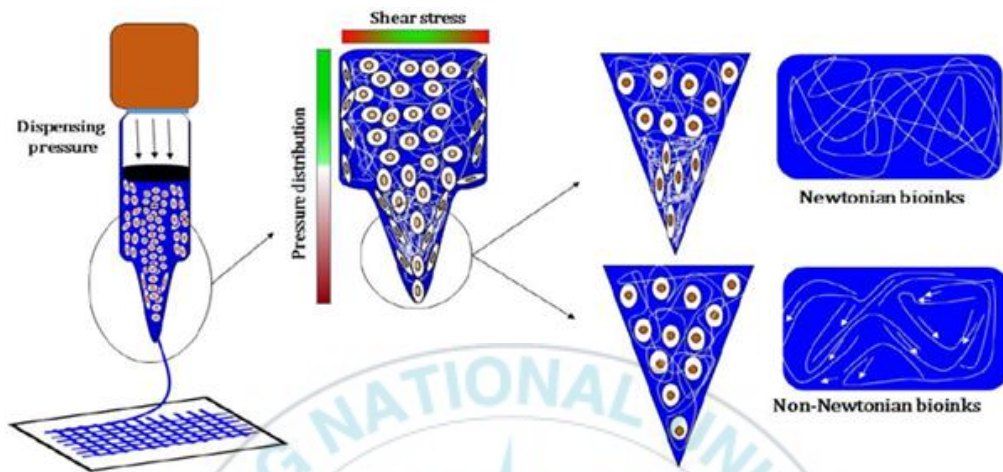
[Figure adapted from Jos Malda (2013). "25th anniversary article: engineering hydrogels for Biofabrication". *Advanced materials*, 25(36), 5011-5028.]

Figure 4. Correlations of factors for 3D bioprinting.



[Figure adapted from David Chimene (2016). "Advanced Bioinks for 3D Printing: A Materials Science Perspective". *Annals of biomedical engineering*, 44(6), 2090-2102.]

Figure 5. Characteristics of advanced bioinks.



[Figure adapted from Amit Panwar (2016). “Current status of bioinks for micro-extrusion-based 3D bioprinting”. *Molecules*, 21(6), 685.]

Figure 6. Properties of Newtonian and non-Newtonian bioinks in the syringe with dispensing pressure.

2. Characterization of the role of nano-hydroxyapatite (nHA) on 3D-printed PCL/nHA composite scaffolds

In orthopedic and dental applications, polycaprolactone (PCL) is one of the most widely used biomaterials due to its low toxicity and high printability [12]. Various PCL-based composite biomaterials integrated with synthetic or natural materials have been explored to overcome intrinsic drawbacks of PCL including hydrophobicity, limited cell adhesion sites, and low biological interactions, [13]. Composites of PCL and nano-hydroxyapatite (nHA), which is a biocompatible nano biomaterial producing excellent interactive conformities to bond with the native bone tissue, have been expansively studied as a biomaterial for 3D printing to optimize biochemical properties of the scaffold for bone regeneration and induce morphological reconstruction. Due to the osteoconductive nature of nHA associated with osteoblast adhesion, the PCL/nHA composite scaffolds enhance bone tissue formation *in vivo* [14]. Yet, in spite of numerous studies performed on 3D-printed PCL scaffolds combined with nHA, the role of nHA in physiochemical and mechanical properties is unclear. Thus, the aim of this study is to evaluate the morphological, physical and biochemical characteristics of nHA in micro-fabricated scaffolds suitable for bone tissue engineering. Therefore, the various effects of nHA in the 3D-printed PCL-based

composite scaffolds were quantitatively assessed by monitoring of changes in mechanical properties as well as cell proliferation and osteoconductivity with different concentrations of nHA.



2.1. Materials and methods

2.1.1. Scaffold fabrication

The scaffolds were fabricated using a custom-made 3D bioprinter named Microextrusion-based 3D bioprinter composed of 3 motion axes, nozzles, extrusion pistons, motion control units, and temperature controllers. PCL (Polysciences, USA, particle size < 600 μm , M.W. = 50,000) and nHA (Sigma-Aldrich, USA, particle size < 200 nm) were blended in a mortar with different ratios of nHA (0, 10, 20 and 30 wt %) and melted in thermally controlled syringes at 70°C. The scaffold was designed in 0°/90° orientation to generate the porous structure in each layer. The nozzle with a diameter of 400 μm was used to fabricate a scaffold measuring 18 mm \times 18 mm \times 2.4 mm.

2.1.2. Physicochemical characterization

The morphological characteristics of the scaffolds were observed by scanning electron microscopy (SEM, VEGA II LSU, TESCAN, Czech) at 5 kV of an accelerating voltage after gold coating. The top and cross-sectional images were captured at 45 \times and 70 \times of magnification each other. Fourier-transform infrared spectroscopy (FT-IR, Spectrum X, PerkinElmer, USA) in a range of 650 to 4000 cm^{-1} and universal testing machine (UTM, LR5K Plus, LLOYD instruments, UK) with 1 mm/min cross-head velocity were used to assess the chemical and mechanical properties of the PCL/nHA

scaffolds. Young's Modulus was calculated in the linear region of the stress-strain curve acquired from triplicate measurements for each nHA concentrations.

2.1.3. Biological activities in PCL/nHA composite scaffolds

The scaffolds were prepared by washing with PBS including 1% penicillin-streptomycin after sterilizing with 70% ethanol for 2 hours each other and then, prewetting in cell culture medium for one day before seeding. Rabbit bone marrow-derived mesenchymal stem cells (MSCs) with a density of 5×10^4 cells/mL were seeded onto each scaffold. After one day, the cell culture medium was changed into osteogenic differentiation medium containing MEM α -modification including 10 % FBS, 1% penicillin-streptomycin, 50 μ g/ml 2-Phospho-L-ascorbic acid trisodium (Sigma Aldrich, USA), 10 mM β -Glycerol phosphate disodium salt pentahydrate (Sigma Aldrich, USA), 100 nM Dexamethasone (Sigma Aldrich, USA). The cell-seeded scaffolds were immersed and cultured in the medium for 21 days. AlamarBlue assay was used to assess cell viability and proliferation in the scaffolds. The cell-seeded scaffolds were washed and cultured with phenol-free cell culture media including 10 % alamarBlue reagent (Invitrogen, USA) for 4 hours. Optical absorbance was measured using a spectrophotometer (Epoch, BioTek., USA) at the wavelengths of 570 nm and 600 nm. The experimental procedures were performed in triplicates for each nHA concentration at 7, 14 and 21 days. The differentiation of MSCs into osteoblasts as well as cell mineralization can be detected by energy dispersive X-ray spectroscopy (EDS, HORIBA, Japan) from the atomic percentage of chemical elements.

2.2. Results and discussion

2.2.1. Physical and chemical properties of PCL/nHA scaffolds

The FT-IR spectra of PCL/nHA scaffolds in accordance with nHA concentration were shown in Figure 7(a). In the spectrum of nHA, the characteristics of the phosphate group (P=O) appeared at the wavelengths of 961 and 1087 cm^{-1} . Spectrum peaks corresponding to nHA were more clearly observed as the concentration of nHA increases in the scaffold, which implies that the 3D fabrication procedures made negligible thermal damage to nHA and maintained the chemical structure of the extruded materials. Also, other peaks including carbonyl group (C=O) at 1721 cm^{-1} and the methane group (C-H) at 2865 and 2943 cm^{-1} were consistently observed, indicating successful incorporation of nHA and PCL in the composite scaffolds.

Mechanical strength of the PCL/nHA composite scaffold was examined as shown in Figure 7(b). It was determined that the Young's Moduli of the PCL/nHA scaffold with 0% nHA, 10% nHA, 20% nHA, and 30% nHA were 54.0758 MPa, 43.6868 MPa, 61.2351 MPa, and 81.7659 MPa, respectively. The Young's moduli of the composite scaffolds incorporated with nHA linearly increased with increasing nHA concentrations. In addition, the scaffolds over 10% nHA had higher strength than the PCL scaffold without nHA, which indicates that the intrinsic strength of nHA can be beneficial to enhance mechanical properties of the composite scaffolds. Compared with other studies for conventional PCL/nHA composite scaffolds fabricated with the freeze-drying method, the tendency of the measured mechanical strength was similar to each other

[15]. Also, it has been known that the material bonding between PCL and nHA is stronger as the smaller particle size allows exposure to larger surface areas [16]. Therefore, as demonstrated in the experimental results, nano-sized hydroxyapatite used in this study can improve the mechanical strength of the scaffold.



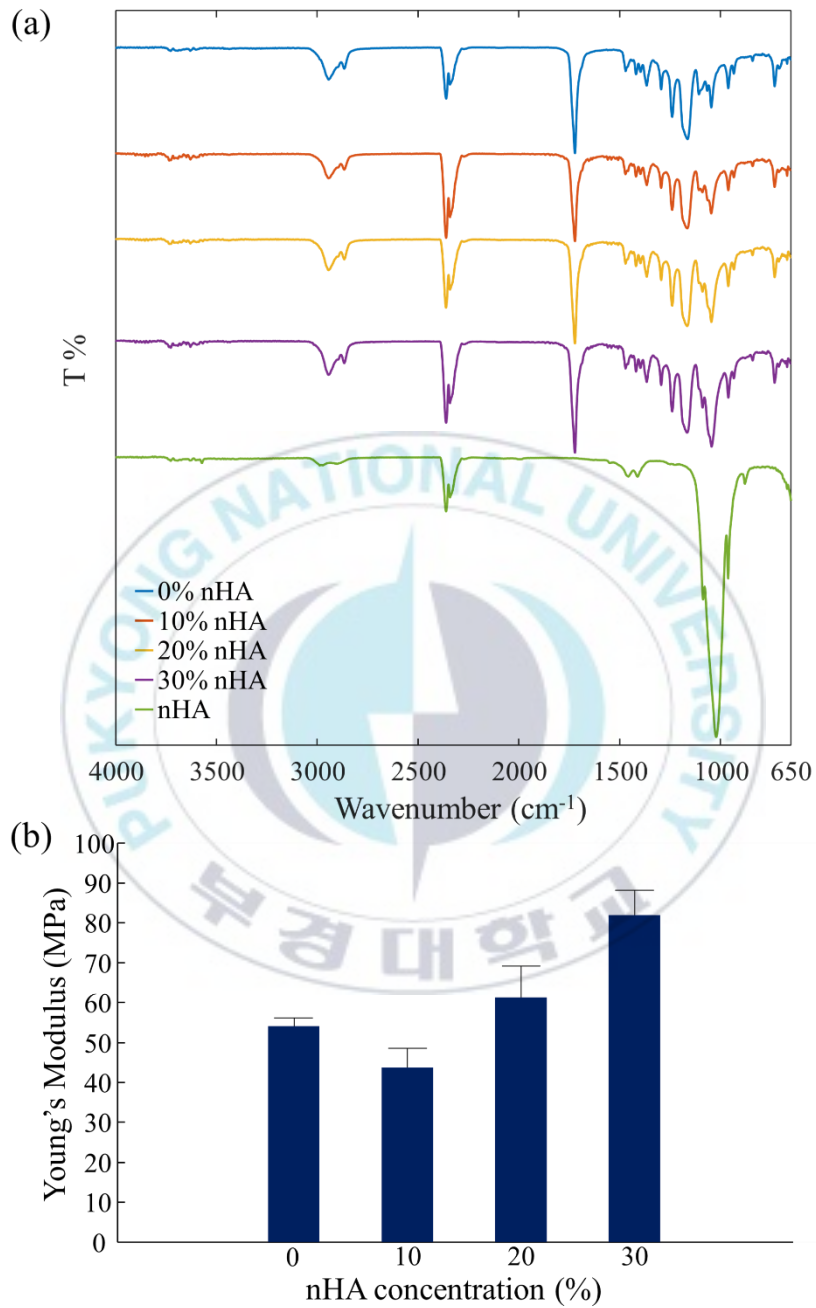
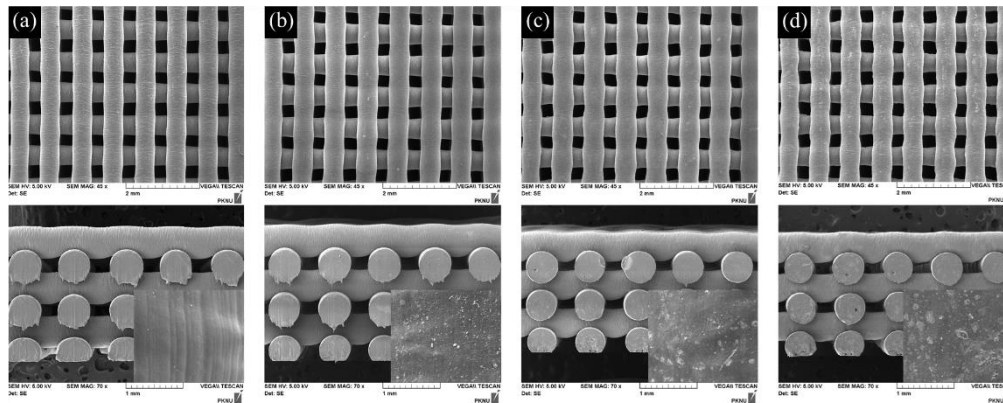


Figure 7. Physicochemical characteristics: (a) FT-IR spectra; (b) Young's moduli of PCL/nHA composite scaffolds with different concentrations of nHA (n=3).

2.2.2. Morphological characterization and printability

The morphology of the 3D-printed scaffolds with different nHA concentrations was observed using SEM as shown in Figure 8. The calculated pore size and strut diameter of each scaffolds were similar regardless of different the nHA concentrations: 295 μm and 540 μm , respectively. It has been demonstrated that the addition of nHA can increase viscoelastic properties including viscosity and shear modulus of composite scaffolds [16]. However, Microextrusion-based 3D bioprinter using piston-driven configuration is less vulnerable to viscoelastic changes than other bioprinting methods including pneumatic-based systems. Thus, although rheological properties vary with the incorporation of nHA, 3D-printed PCL/nHA composite scaffolds shown in Figure 8 had similar resolution and pore size in the same printing condition. Also, it was confirmed that the surface roughness of the PCL/nHA composite scaffolds increases as the concentration of nHA increases, which can be beneficial to cell attachment.



(e)	0%	10%	20%	30%
Strut diameter [μm]	540.79 ± 44.24	541.41 ± 46.42	541.52 ± 44.76	540.81 ± 43.09
Pore size [μm]	295.6 ± 52.5	293.94 ± 55.23	294.75 ± 53.88	296.51 ± 50.78

Figure 8. SEM images of the top, side, and surface views of the PCL/nHA composite scaffolds: (a) 0% nHA; (b) 10% nHA; (c) 20% nHA; (d) 30% nHA; (e) Strut diameter and pore size of the composite scaffolds.

2.2.3. Cell-scaffold interaction

Cell proliferation changes in the PCL/nHA composite scaffolds were monitored over 21 days using the alamarBlue assay and is represented in Figure 9(a). It was demonstrated that MSCs were more proliferative as the concentration of nHA in the composite scaffolds increased. The experimental results imply that cellular interactive cues from the micro-environment of nHA can enhance the viability and proliferation of cells in the PCL/nHA composite scaffolds. EDS analysis shown in Figure 9(b) and (c) indicated the differentiation of MSCs into osteoblasts and subsequent mineralization in the scaffolds. The content of mineralization (calcium and phosphorous) increased linearly from day 0 to day 14 in the scaffold with 20% and 30% nHA. Furthermore, the mineralized tissue formed in 20% HA scaffold exhibited a Ca/P ratio of 1.8 closely resembling to that of the natural bone apatite [17]. The result indicates that calcium and phosphorous released from nHA incorporated in the scaffold can enhance the cell-material interaction and induce incremental changes in mineralization and osteoconductivity.

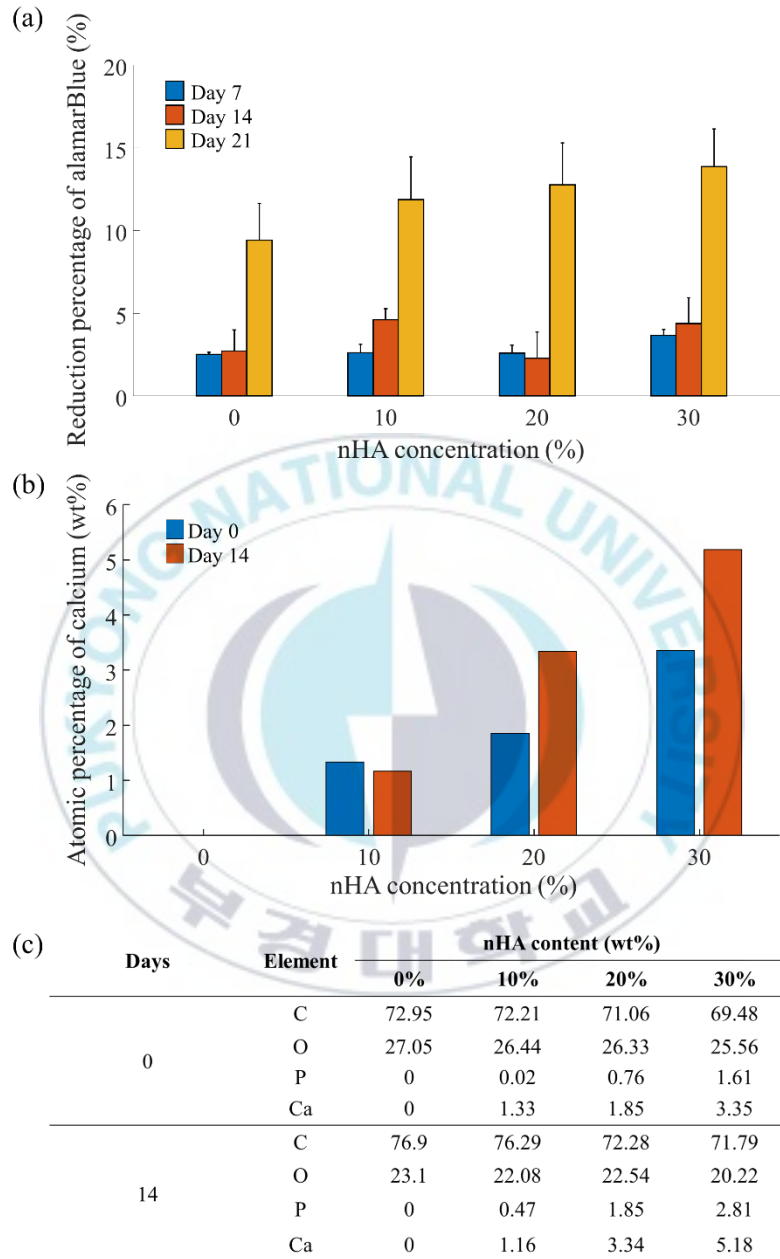
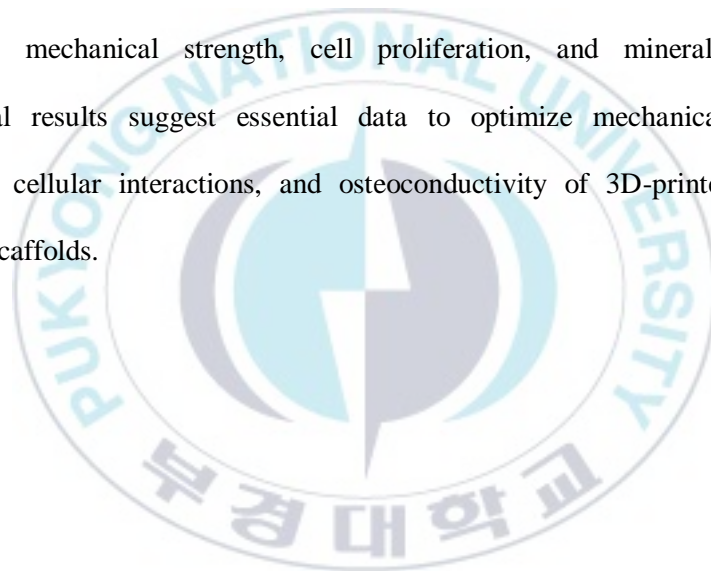


Figure 9. Biological activities in PCL/nHA composite scaffolds: (a) Cell proliferation with alamarBlue reagent; (b) Mineralization on the PCL/nHA composite scaffolds; (c) Atomic percentage of chemical elements in the PCL/nHA composite scaffolds.

2.3. Conclusion

The results of this study demonstrate the physiochemical and mechanical effects of nHA in the PCL/nHA composite scaffolds fabricated using Microextrusion-based 3D bioprinter. The nHA was successfully incorporated in the PCL/nHA composite scaffolds up to 30% of nHA without significant changes in scaffold morphology and chemical composition. Also, the addition of nHA in the scaffolds made incremental changes in mechanical strength, cell proliferation, and mineralization. The experimental results suggest essential data to optimize mechanical properties, printability, cellular interactions, and osteoconductivity of 3D-printed PCL/nHA composite scaffolds.



3. Enhanced 3D printability of alginate-based hydrogels with carrageenan

Hydrogels have been used for the most popular biomaterial to create 3D tissue-engineered structures for mimicking native extracellular matrix (ECM) and providing adequate environments for cell behaviors with the appropriate porosity, pore size, interconnectivity, and biocompatibility [10, 18]. Also, the hydrogels with shear thinning properties have been most widely used in extrusion-based bioprinting because randomly arranged polymer chains of the hydrogels can be aligned and become extrudable by applying shear forces [19]. Therefore, it has been demonstrated in many studies that the rheological properties of the hydrogel play an important role in controlling the resolution and shape fidelity of the 3D-bioprinted structures [20, 21]. Based on rheological characteristics of the hydrogels including shear thinning and thixotropic behaviors, printing parameters such as printing speed, pressure, and nozzle size can be optimized [22].

Among several hydrogels, the alginate-based hydrogel is one of the most widely used biomaterials in biomedical applications because of low cost and decent biocompatibility and multiple crosslinking methods [23]. However, extrusion-based bioprinting of alginate suffers from low shear modulus and unstable crosslinking, which make challenging to obtain well-controlled shapes and maintain the 3D-printed structures [24]. To overcome these limitations, other additives, such as graphene oxide,

silica, and cellulose nanofibers, have been used for strengthening the mechanical properties of the alginate-based hydrogels [25]. Yet, these additives in the tissue-engineered scaffolds often lead to other problems related to long-term safety, biodegradability, and cost-effectiveness.

Carrageenan has been widely used for gelling, thickening and stabilizing in food and pharmaceutical applications [26]. It is a natural polysaccharide extracted from red algae and consists of repeatedly (1-3)-linked β -D-galactose and (1-4)-linked α -D-galactose units [27]. Moreover, the carrageenan is classified into three types based on the number of sulfate groups, i.e. kappa (κ), iota (ι) and lambda (λ), and these sulfate groups in the backbone provide a positive influence on cell adhesion, cell proliferation, and cell differentiation [28]. Also, it was reported that carrageenan inhibits inflammatory responses because of negatively charged carboxyl and sulfate groups [18]. In addition, the composition of carrageenan shows similarity with mammalian glycosaminoglycans in a component of ECM [29]. Due to these advantages, many researchers have used carrageenan for encapsulation of diverse cell types, drug delivery and cartilage regeneration for preclinical and clinical uses. Several studies tried to bring the advantages of carrageenan to fabricate tissue-engineered scaffolds using conventional tissue engineering techniques [30, 31], but few papers regarding 3D bioprinting using carrageenan composites were published. In this study, the goal is to present the feasibility of precise fabrication of alginate/carrageenan composite scaffolds based on a precise assessment of rheological properties, printability, and 3D deposition using a custom-made extrusion-based 3D bioprinting. At first, the proper concentration of

calcium sulfate was determined by the assessment of shear modulus of alginate-based hydrogels with various levels of ionic crosslinking. Moreover, alginate/carrageenan composite hydrogels were prepared with four different concentrations of carrageenan and used to measure their rheological properties. Based on the assessed viscoelasticity of alginate and alginate/carrageenan hydrogels, printing resolutions in different printing parameters including printing speed and pressure were simulated and presented in the printability maps. In addition, alginate and alginate/carrageenan scaffolds were bioprinted with various printing parameters and used to compare their printability with the simulated results. Also, 3D deposition of both alginate and alginate/carrageenan hydrogels were assessed and compared with each other by continuous monitoring of shape fidelity in 3D structures in ten layers and similar printing resolution. Finally, the cell viability of the 3D alginate/carrageenan composite scaffolds, printed with mesenchymal stem cells using optimized printing parameters, was evaluated using live/dead staining and confocal fluorescence imaging.

3.1. Materials and methods

3.1.1. Hydrogel preparation

Sodium alginate (Alg) was purchased from Sigma-Aldrich Inc., USA, and the final concentration of Alg solution was fixed at 2% w/v in this study. The carrageenan (Carr), mainly composed of κ -Carr, was also obtained from Sigma-Aldrich Inc., USA. The Carr at the concentrations of 0.5, 1.0, and 1.5% w/v was mixed with Alg solution. Calcium sulfate (CaSO_4 , Sigma-Aldrich Inc., USA) was used as the crosslinking agent for Alg solution. The CaSO_4 solution was prepared with several concentrations (0.5, 1.0, 1.5, 2.0, and 3.0% w/v) to determine the optimal concentration for maximizing mechanical properties. The prepared CaSO_4 solution was added to Alg-Carr composite hydrogel. All solutions were dissolved in deionized water refined by RiOs™ water purifier (Millipore, France). The Alg- CaSO_4 and Alg-Carr- CaSO_4 composite hydrogels were homogeneously mixed using a three-way stopcock.

3.1.2. Rheological evaluation

The rheological properties of various concentrations of Alg- CaSO_4 and Alg-Carr- CaSO_4 composite hydrogel were measured using a rheometer (HR-2, TA Instruments, USA) with a 20 mm parallel plate at a constant temperature of 25°C. All rheological experiments were performed in triplicate. To assess rheological properties for optimizing printing parameters, shear rate sweep test, frequency sweep test, and

recovery test were performed. For various shear thinning materials including alginate-based hydrogels, the power law model has been widely used to analyze the viscoelastic properties [32]. Power law index (n) and zero viscosity (η_0) are calculated from the shear rate-viscosity curve of shear rate sweep test. The printing parameters such as pressure and printing speed are calculated from the power-law index equation, described below:

$$\eta = \eta_0 \dot{\gamma}^{n-1}$$

where η is shear viscosity, $\dot{\gamma}$ is the shear rate, and η_0 is viscosity at the reference shear rate called zero viscosity [33]. The viscosity (η) of the composite hydrogels were assessed using the shear rate sweep test in the shear rate range of 0.01-1000 s^{-1} . Frequency sweep test was performed in the angular frequency of 0.1-500 rad/s at a strain in the linear viscoelastic region where the test is performed without destroying the structure of the sample to assess the storage modulus (G') and the loss modulus (G''). The recovery test was performed to compare the recovering abilities of the samples in three sections: (1) the shear rate of 0.1 s^{-1} for 60 seconds, (2) the shear rate of 100 s^{-1} for 10 seconds, and (3) the shear rate of 0.1 s^{-1} for 60 seconds.

3.1.3. Printability simulation and assessment

As previously described for the extrusion-based bioprinting for a nozzle diameter D and the pressure drop ΔP within the nozzle length L , the flow rate can be expressed as [34]:

$$Q = \left(\frac{\pi n}{3n + 1} \right) \left(\frac{\Delta P}{2\eta_0 L} \right)^{\frac{1}{n}} \left(\frac{D}{2} \right)^{\frac{3n+1}{n}}$$

Also, the flow rate can be determined using the printing speed v_n and the printed diameter D_p , assuming a perfect cylindrical form, as follows:

$$Q = \frac{V}{t} = \left(\pi \left(\frac{D_p}{2} \right)^2 l \right) \frac{1}{t} = \frac{\pi D_p^2 v_n}{4}$$

where V is the printed volume, t is the printed time, and l is the printed length. Using these two equations, the printed diameter can be calculated under the given bioprinting conditions, including the shear-thinning properties, the printing speed, the nozzle diameter, and the pressure change, as follows:

$$D_p = 2 \sqrt{\frac{Q}{\pi v_n}}$$

The printability was simulated by comparing the printed diameter with the nozzle diameter based on the previous theoretical work [35]. The printability simulation map was created by presenting the calculated printability in log scale with various printing speed (0-16 mm/s) and pressure (10-60 kPa) for both Alg and Alg/Carr composite hydrogels. Therefore, the ideal printability, indicating that the printed diameter is the same as the nozzle diameter, was represented as zero.

3.1.4. Bioprinting

The prepared hydrogels were printed using Microextrusion-based 3D bioprinter, composed of 3 motion axes (x, y, and z), a temperature controller (< 200°C), and a pneumatic controller (< 700 kPa). Single struts of Alg-CaSO₄ and Alg-Carr-CaSO₄ were printed at various combinations of printing velocities (1, 2, 4, 8, and 16 mm/s) and extrusion pressures (20, 25, 30, 35, 40, 45, and 50 kPa) through the nozzle with an inner diameter of 0.51 mm.

3.1.5. Evaluation of 3D deposition fidelity

3D deposition of Alg-CaSO₄ and Alg-Carr-CaSO₄ were evaluated and compared against each other with printing parameters for the subequal strut diameters (Alg-CaSO₄: 4 mm/s, 30 kPa and Alg-Carr-CaSO₄: 2 mm/s, 50 kPa). The deposition fidelity of Alg-CaSO₄ and Alg-Carr-CaSO₄ was assessed by printing a 13.2 mm × 13.2 mm square-shaped 3D structure with ten layers.

3.1.6. Bioprinting of Alg-Carr-CaSO₄ with stem cells

The rabbit adipose-derived mesenchymal stem cells were used to demonstrate cell viability in 3D-printed Alg-Carr-CaSO₄ composite hydrogels with fixed concentrations of 1% CaSO₄ and 1.5% Carr. The cells were cultured in α -minimum essential medium modification (Hyclone Inc., USA) including 10% fetal bovine serum (FBS, Corning Inc., USA) and 1% penicillin-streptomycin (Corning Inc., USA) at 37°C in a

humidified atmosphere of 5% CO₂. The cells with a final density of 5×10^5 cells/mL were cultured on Alg-CaSO₄ and Alg-Carr-CaSO₄ composite scaffolds. The rectangular 3D-bioprinted scaffold was fabricated in 0°/90° orientation on 35 Ø cell culture dish (size: 25 mm × 25 mm, line space: 1.3 mm, layer: 4, nozzle diameter: 0.51 mm).

3.1.7. Cell viability

At first, the 3D-bioprinted Alg-Carr-CaSO₄ scaffold was immersed in 4% aqueous solution of calcium chloride (CaCl₂, Duksan Pure Chemicals CO., Korea) for one minute and washed three times using phosphate buffered saline (PBS, Corning Inc., USA). After this, the cell culture medium was introduced into the scaffold and cultured at 37°C in 5% CO₂ in a humidified incubator. To evaluate cell viability and proliferation in the scaffolds, alamarBlue assay was used during three days. The 3D-bioprinted scaffolds were cultured with 10% alamarBlue reagent (Invitrogen, USA) for four hours in the incubator. Optical absorbance was measured using a spectrophotometer (Epoch, BioTek., USA) at the wavelengths of 570 nm and 600 nm. The experiment was performed in ten samples for each Alg-CaSO₄ and Alg-Carr-CaSO₄ scaffolds. The fluorescent live/dead cell staining was performed on the scaffold using fluorescein diacetate (FDA, Sigma-Aldrich Inc., USA) and propidium iodide (PI, Sigma-Aldrich Inc., USA). The 3D-bioprinted Alg-Carr-CaSO₄ composite scaffold was washed three times with PBS and then stained with FDA and PI working solutions for 5 minutes at room temperature as per the manufacturer's instructions. The stained scaffold was three-dimensionally scanned by confocal laser scanning microscope (LSM 700, Carl

Zeiss, Germany) in 100× magnification. The live/dead image of Alg-Carr-CaSO₄ scaffold was created by projecting with 300 slides of single images obtained by z-stack acquisition using ImageJ software.



3.2. Results and discussion

3.2.1. Rheological characterization of Alg-CaSO₄

The frequency sweep test was carried out with different concentrations of CaSO₄ with 2% Alg solution to characterize the influence of CaSO₄ on the mechanical strength of the hydrogel. In Figure 10(a), the storage modulus G' and loss modulus G'' are shown for different concentrations of CaSO₄ to determine the optimum CaSO₄ concentration for highest mechanical strength. The 0% CaSO₄ in Alg has lower G' than G'' , which indicates the 2% Alg is close to the liquid state at this CaSO₄ concentration. In Figure 10(b), storage moduli for different CaSO₄ concentration are compared at the angular frequency of 1 rad/s. The storage moduli of the Alg hydrogel increased until 1% CaSO₄ concentration and then it decreased. Thus, 1% CaSO₄ was selected for further experiments with 2% Alg solution.

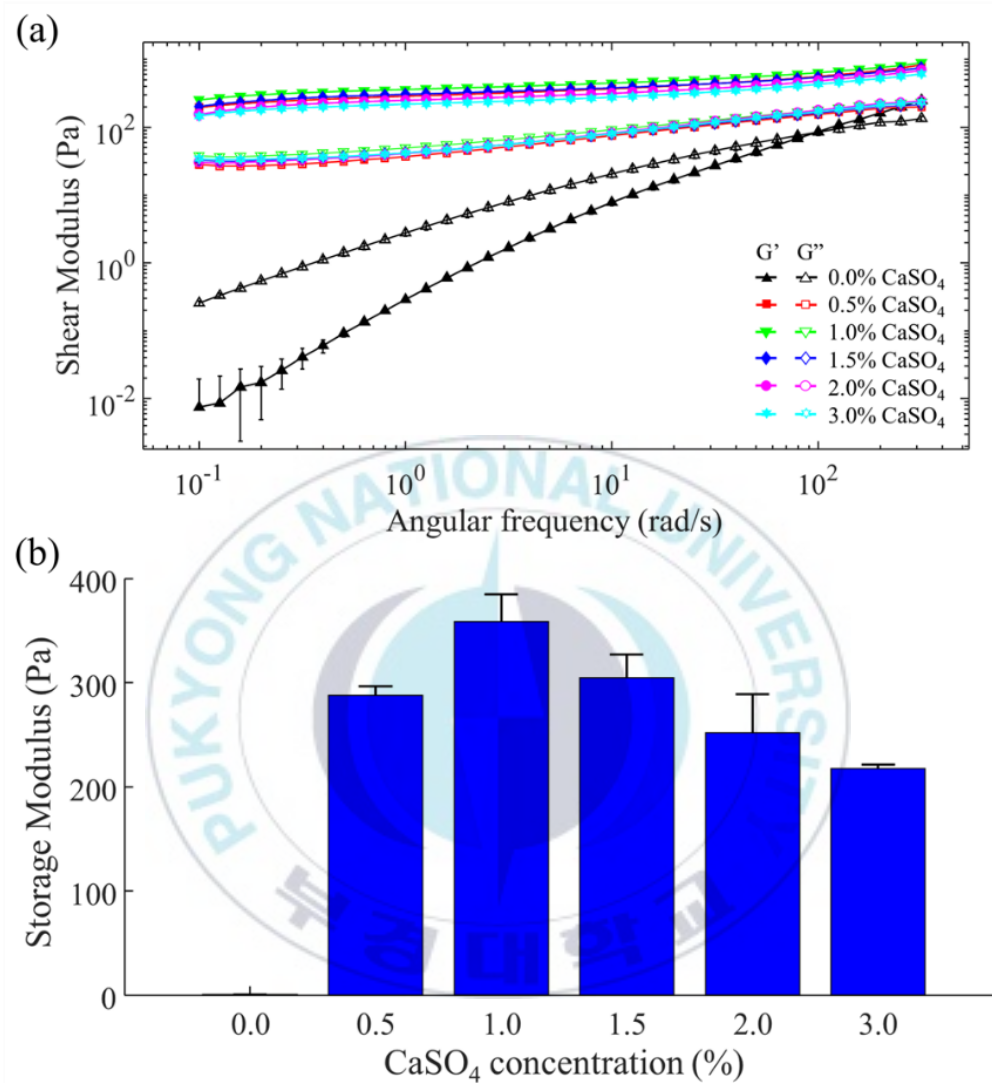


Figure 10. Rheological assessment of Alg crosslinked with CaSO₄: (a) Shear moduli of Alg-CaSO₄; (b) Storage moduli at an angular frequency of 1 rad/s with different concentrations of CaSO₄.

3.2.2. The effects of Carr on rheological characteristics of Alg-CaSO₄ hydrogel

The rheological study was performed with Carr concentrations of 0.5%, 1.0%, 1.5% and 1% CaSO₄ content to evaluate the effects on viscoelastic properties of Alg-CaSO₄ and its printability. The effects on viscosity and shear modulus of Carr concentration are illustrated in Figure 11, 12, and 13. Figure 11 and 12 show the viscosity and shear modulus of the Alg-CaSO₄ hydrogel were augmented with increasing Carr concentrations without sacrificing of shear thinning properties. At 1 rad/s angular frequency, as shown in Figure 12(b), the maximum storage modulus of Alg-CaSO₄ was obtained at the highest Carr concentration (1.5%), which implies potential uses of Carr for improvement of viscoelastic properties and printability of alginate-based bioink. When the hydrogel is printed, the structure of the crosslinked hydrogel might be broken due to the high shear rate in the nozzle. Thus, the thixotropic property of the hydrogel is essential to use it for extrusion-based bioprinter. Therefore, the recovery time of Alg-Carr-CaSO₄ composite hydrogel was measured through three steps: low – high – low shear rate as shown in Figure 13. The recovery behavior of Alg-Carr-CaSO₄ composite hydrogel was examined at a shear rate of 0.1 s⁻¹ for 60 seconds to mimic the stationary state of a syringe barrel before printing as shown in section 1 of Figure 13, and at 100 s⁻¹ for 10 seconds to mimic the state in a nozzle during printing as shown in section 2 of Figure 13. Lastly, section 3 mimics the state after printing at the same condition as section 1. The recovery times of the Alg-Carr-

CaSO₄ composite hydrogels were calculated to be 13 seconds in 0% Carr, 15 seconds in 0.5% Carr, 8 seconds in 1.0% Carr, and 5 seconds in 1.5% Carr. Thus, as the concentration of Carr increased, the viscosity and mechanical properties were improved while recovery time was decreased. These rheological properties can help to maintain the layer-by-layer structure printed with Alg-Carr-CaSO₄ composite hydrogel without any collapsing situation.



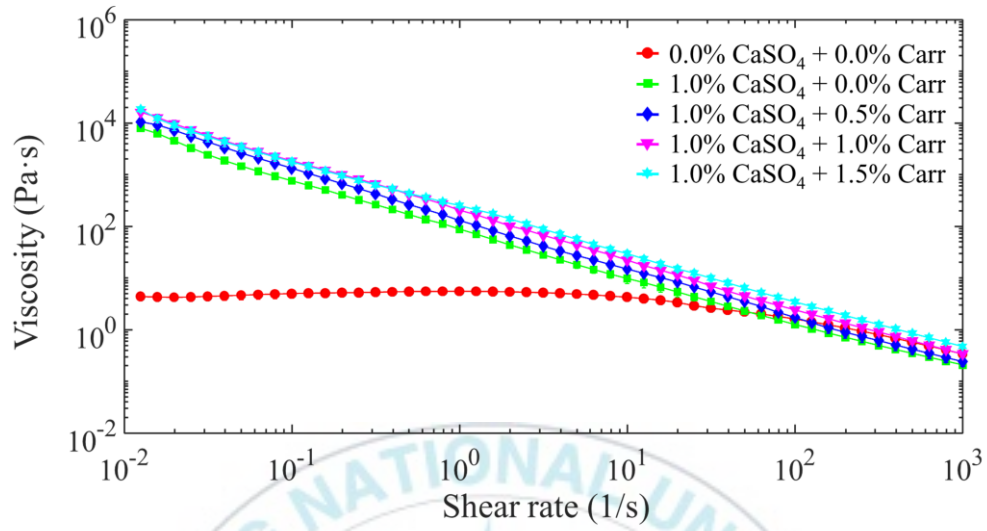


Figure 11. Flow curves of the shear rate sweep test of the Alg-Carr-CaSO₄ as a function of shear rate (0.01-1000 s⁻¹).

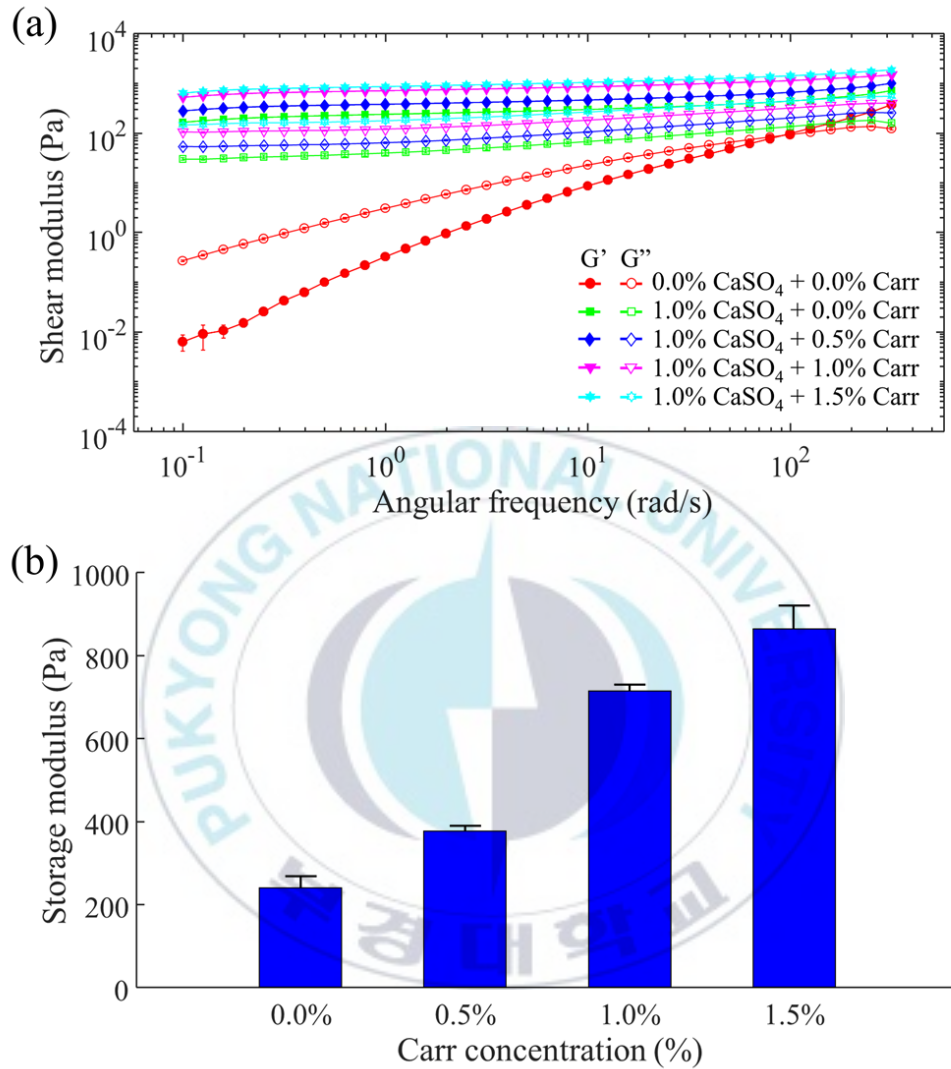


Figure 12. Rheological assessment of Alg-Carr-CaSO₄: (a) Frequency sweep test of the Alg-Carr-CaSO₄ (0.1-500 rad/s); (b) Storage modulus at 1 rad/s angular frequency.

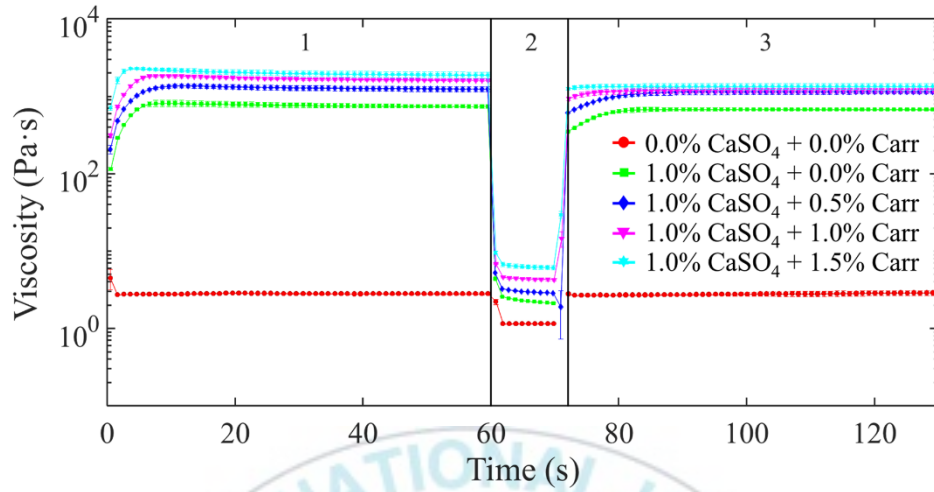
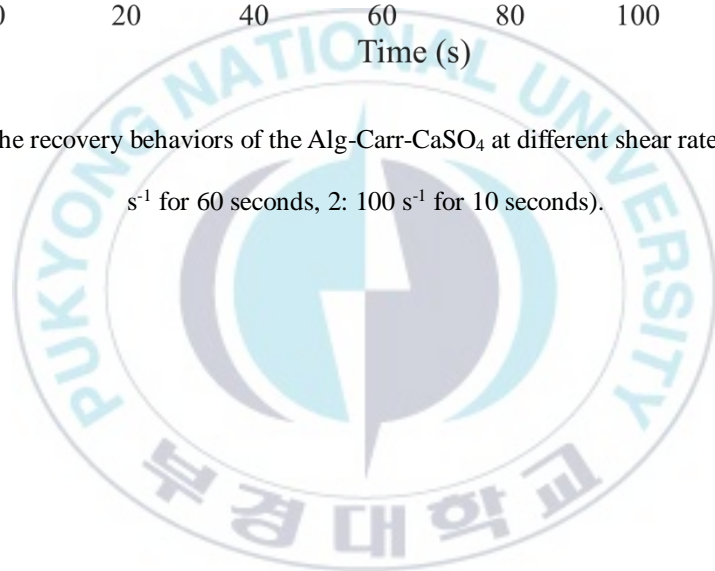


Figure 13. The recovery behaviors of the Alg-Carr-CaSO₄ at different shear rates (1 and 3: 0.1 s⁻¹ for 60 seconds, 2: 100 s⁻¹ for 10 seconds).



3.2.3. Printability of Alg-CaSO₄ hydrogel

Printability of the hydrogel was simulated to present printing conditions with various printing parameters and predict optimal printing parameters based on measured rheological properties. Power law index and zero viscosity of Alg-CaSO₄ hydrogel were determined ($n = 0.165$ and $\eta_0 = 65.944$ Pa·s) using the viscosity-shear rate graph obtained in the shear rate sweep test. The printability was calculated and shown in Figure 14(b) with the printing speed of 0-16 mm/s and pressure of 10-60 kPa using the equations described above. The cross marks on the printability map represent the actual printing conditions shown in Figure 14(a) and they were labelled with the printing numbers from 1 to 25. The same labelled numbers in Figure 14(a) and Figure 14(b) indicate the same printing conditions with the same printing speed and pressure in both simulated and actual bioprinting of the Alg-CaSO₄ hydrogel. Also, Figure 14(a) shows microscopic images of the printed struts at various nozzle velocities (1, 2, 4, 8 and 16 mm/s) and pressures (20, 25, 30, 35 and 40 kPa). The obtained microscopic images were quantitatively analyzed to measure the printing resolution and quality which are shown in Figure 15(a) and Figure 15(b). In Figure 14(a), the images with the printing number 2, 3, 4, 5, 8, 9, 10, 14, 15 and 20 show non-uniform or snapped struts because of inadequate printing speed or pressure. On the other hand, at the printing number 11, 16, 17, 21, 22 and 23, the printing resolution is significantly poor with the printing diameter more than 1 mm and the printability more than 2. In Figure 14(b), the printability values around zero (red zone) indicate a

suitable region for precise printing of the Alg hydrogel. Especially, actual printing quality shown in Figure 14(a), 15(a), and 15(b) was high with the printing parameters at the printing numbers 1, 6, 7, 12, 13, 18, 19, 24 and 25 located nearby the red zone in Figure. 14(b), which implies that simulated and actual printability of Alg hydrogel were matched well. In further 3D deposition experiment, printing parameters at the printing number 13 were set up with the strut diameter of 0.758 mm at the printing speed of 4 mm/s and the pressure of 30 kPa.



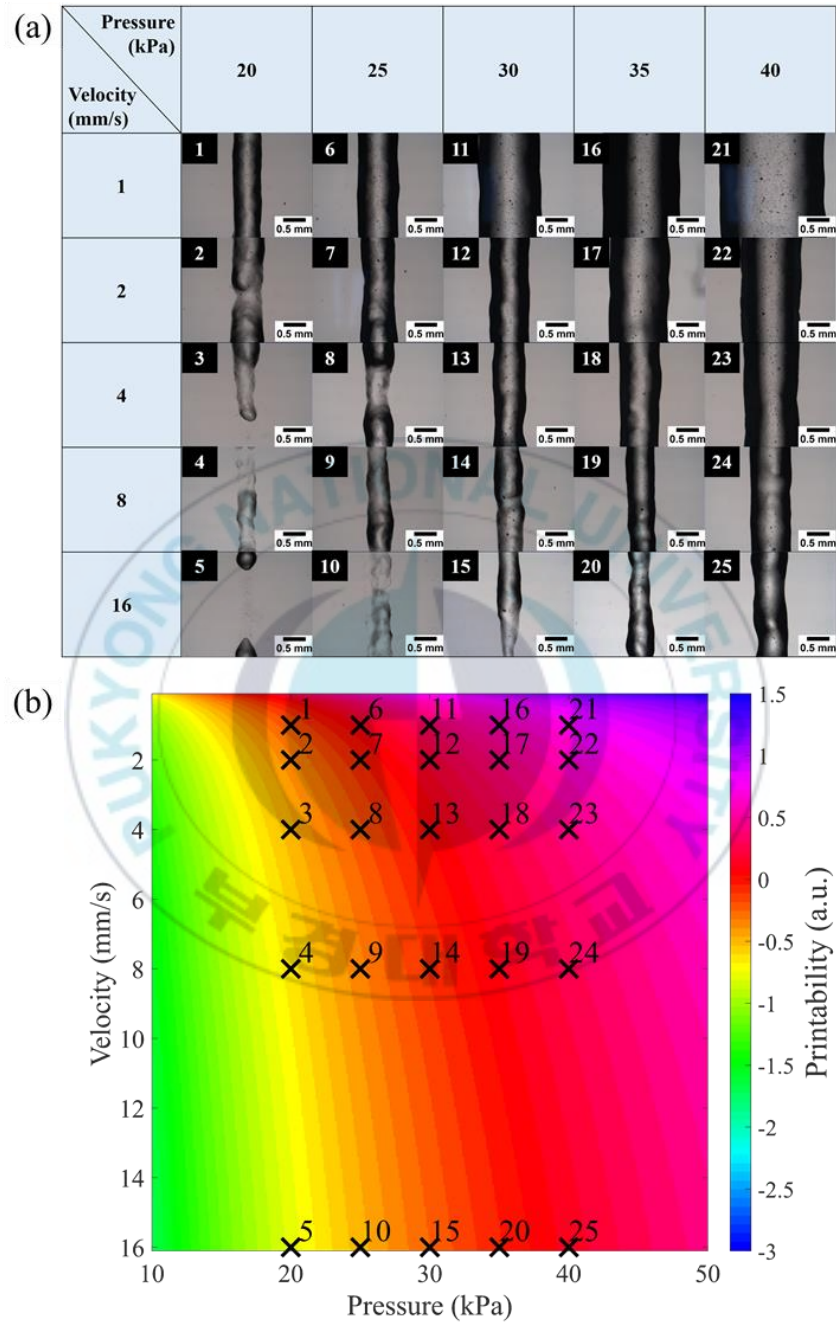
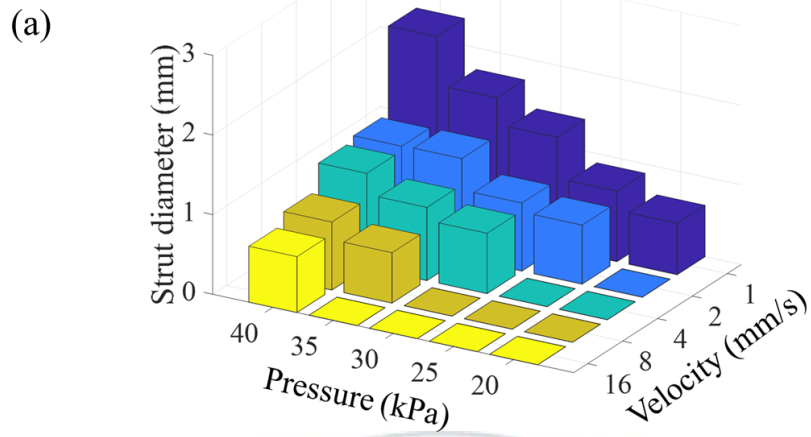


Figure 14. Printability simulation and measurement of Alg-CaSO₄: (a) Microscopic images of printed struts at different printing parameters; (b) Printability simulation of Alg-CaSO₄.



(b)

Pressure (kPa) \ Velocity (mm/s)	20	25	30	35	40
1	0.645±0.034	0.884±0.026	1.398±0.027	1.729±0.027	2.336±0.022
2	N/A	0.741±0.044	0.855±0.022	1.249±0.081	1.240±0.099
4	N/A	N/A	0.758±0.058	0.918±0.047	1.182±0.033
8	N/A	N/A	N/A	0.632±0.039	0.854±0.050
16	N/A	N/A	N/A	N/A	0.701±0.071

Figure 15. Strut diameter of printed Alg-CaSO₄: (a) Printed strut diameter (mm) represented as the average ± standard deviation (n = 10); (b) 3D diagram of printed strut diameter averages.

3.2.4. The effects of Carr on the printability of Alg-CaSO₄ hydrogel

The printability simulation shown in Figure 16(b) was carried out for the Alg-Carr-CaSO₄ hydrogel using the calculated power law index and zero viscosity ($n = 0.102$ and $\eta_0 = 232.576 \text{ Pa}\cdot\text{s}$) by the similar methods previously described above. In addition to the printing parameters applied in Alg-CaSO₄ (Figure 14 and 15), pressures of 45 kPa and 50 kPa were applied as well in the printing of Alg-Carr-CaSO₄ due to its relatively higher viscosity and shear modulus than Alg-CaSO₄. Also, the microscopic images of the printed struts of the Alg-Carr-CaSO₄ hydrogel were captured and quantitatively analyzed as shown in Figure 16(a), 17(a), and 17(b) using similar methods for Alg-CaSO₄. In Figure 16(b), the red zone of Alg-Carr-CaSO₄ composites near the optimum printing parameters was located at higher pressure ranges than those Alg-CaSO₄ in Figure 14(b) due to the enhanced shear modulus. Printing numbers 21, 26, 27, 32 and 33 were located near the red zone in Figure 16(b). The experimental results in Figure 16 and 17 indicate that the printability of actual bioprinting of Alg-Carr-CaSO₄ composite hydrogel was matched well with the simulated results, which implies the potential of printability prediction of shear thinning hydrogels based on rheological assessments. For further evaluation of 3D deposition using Alg-Carr-CaSO₄, the strut diameter of 0.801 mm at the printing speed of 2 mm/s and the pressure of 50 kPa (printing number 32) were set as the printing condition.

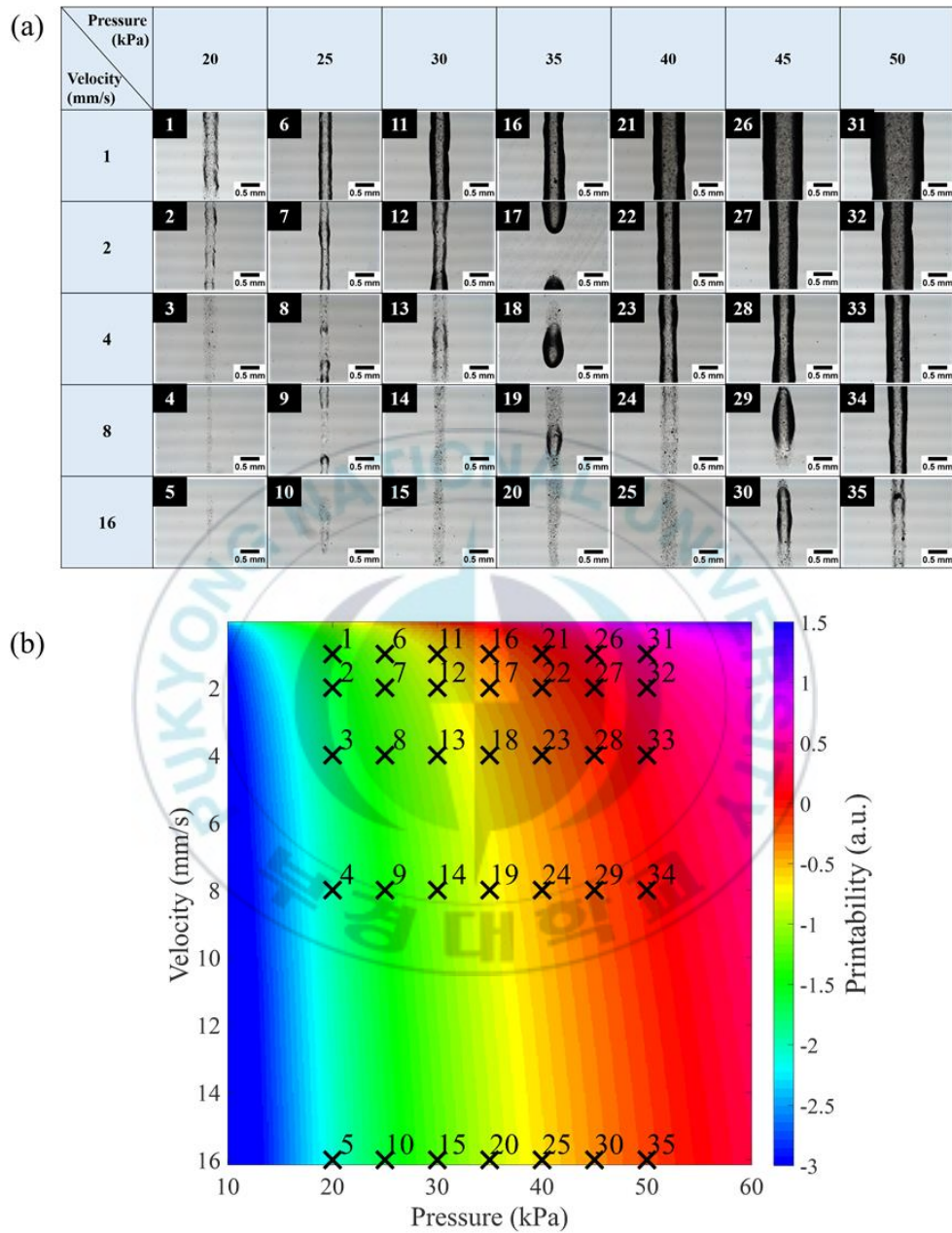
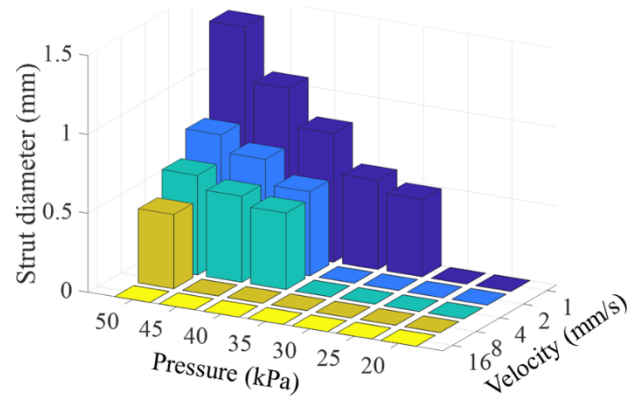


Figure 16. Printability simulation and measurement of Alg-Carr-CaSO₄: (a) Microscopic images of printed struts at different printing parameters; (b) Printability simulation of Alg-Carr-CaSO₄.

(a)



(b)

Pressure (kPa) \ Velocity (mm/s)	20	25	30	35	40	45	50
1	N/A	N/A	0.490±0.032	0.564±0.033	0.816±0.030	1.055±0.009	1.398±0.027
2	N/A	N/A	N/A	N/A	0.534±0.061	0.693±0.054	0.801±0.018
4	N/A	N/A	N/A	N/A	0.485±0.018	0.545±0.036	0.632±0.023
8	N/A	N/A	N/A	N/A	N/A	N/A	0.470±0.033
16	N/A	N/A	N/A	N/A	N/A	N/A	N/A

Figure 17. Strut diameter of printed Alg-Carr-CaSO₄: (a) Printed strut diameter (mm) represented as the average ± standard deviation (n = 10); (b) 3D diagram of printed strut diameter averages.

3.2.5. Assessment of 3D deposition of Alg-CaSO₄ and Alg-Carr-CaSO₄ composite hydrogel

As presented above in the experimental results, it was demonstrated that Carr significantly enhanced the mechanical strength as well as thixotropic properties of the Alg hydrogel. Based on the assessment shown in Figure 15 and Figure 17, the printing parameters for injecting Alg-CaSO₄ (4 mm/s, 30 kPa) and Alg-Carr-CaSO₄ (2 mm/s, 50 kPa) were applied to monitor their 3D deposition with similar printing resolutions of 0.758 ± 0.058 mm and 0.801 ± 0.018 mm, respectively. The effect of Carr on maintaining 3D-printed structure was investigated by continuous monitoring of bioprinted structures of Alg-CaSO₄ and Alg-Carr-CaSO₄. The square-shaped multi-layer structure (13.2 mm × 13.2 mm, 10 layers) was printed as shown in Figure 18. The Alg-CaSO₄, which has relatively low mechanical properties, could only accumulate up to three layers before the wall of the structure collapsed, while Alg-Carr-CaSO₄ could build all layers with high fidelity.

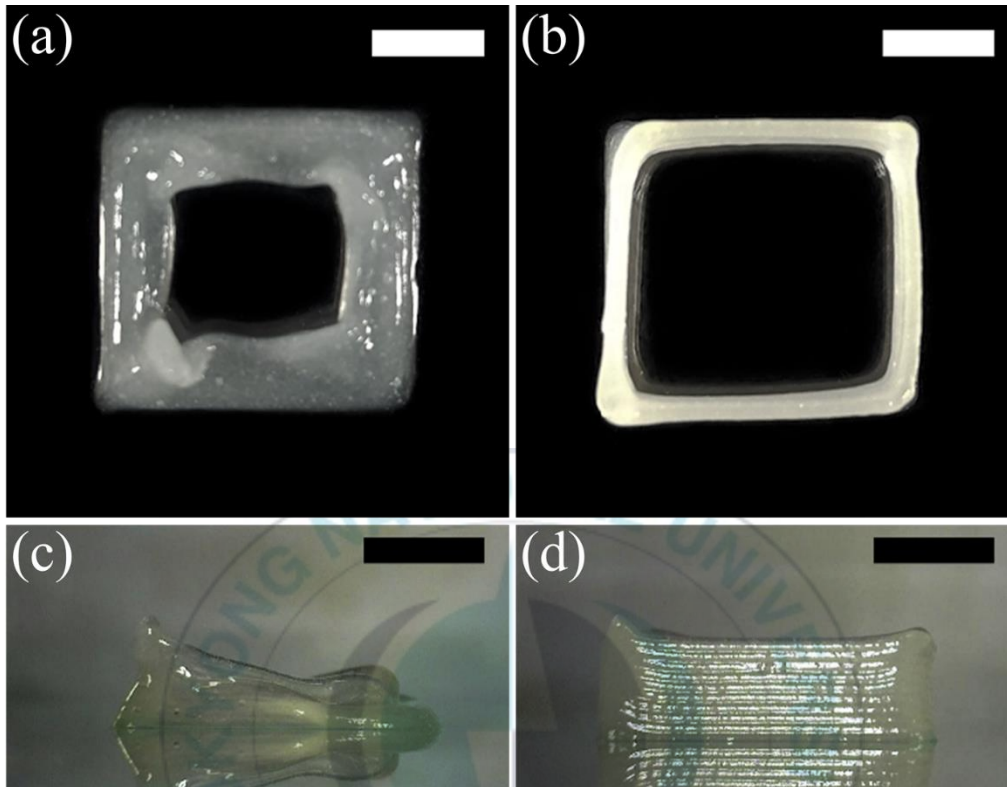


Figure 18. Assessment of 3D deposition: (a and c) Top and side views of 3D deposition of Alg-CaSO₄; (b and d) Alg-Carr-CaSO₄ (Scale bar: 5 mm).

3.2.6. Biocompatibility of bioprinted scaffolds

The cell proliferation changes in Alg-CaSO₄ and Alg-Carr-CaSO₄ scaffolds were monitored using alamarBlue reagent as shown in Figure 19(a). It was indicated that the mesenchymal stem cells exhibited more proliferation in the scaffolds with Carr than scaffolds without Carr. Figure 19(b) shows the fluorescence images of live (green) and dead (red) mesenchymal stem cells in Alg-Carr-CaSO₄ scaffolds obtained by projecting with 300 slides of images scanned by confocal laser scanning microscope. The figure presents that the majority of the encapsulated mesenchymal stem cells were viable after 24 hours and the presence of dead cells was negligible, which implies that the derived hydrogel was cyto-compatible and non-toxic.



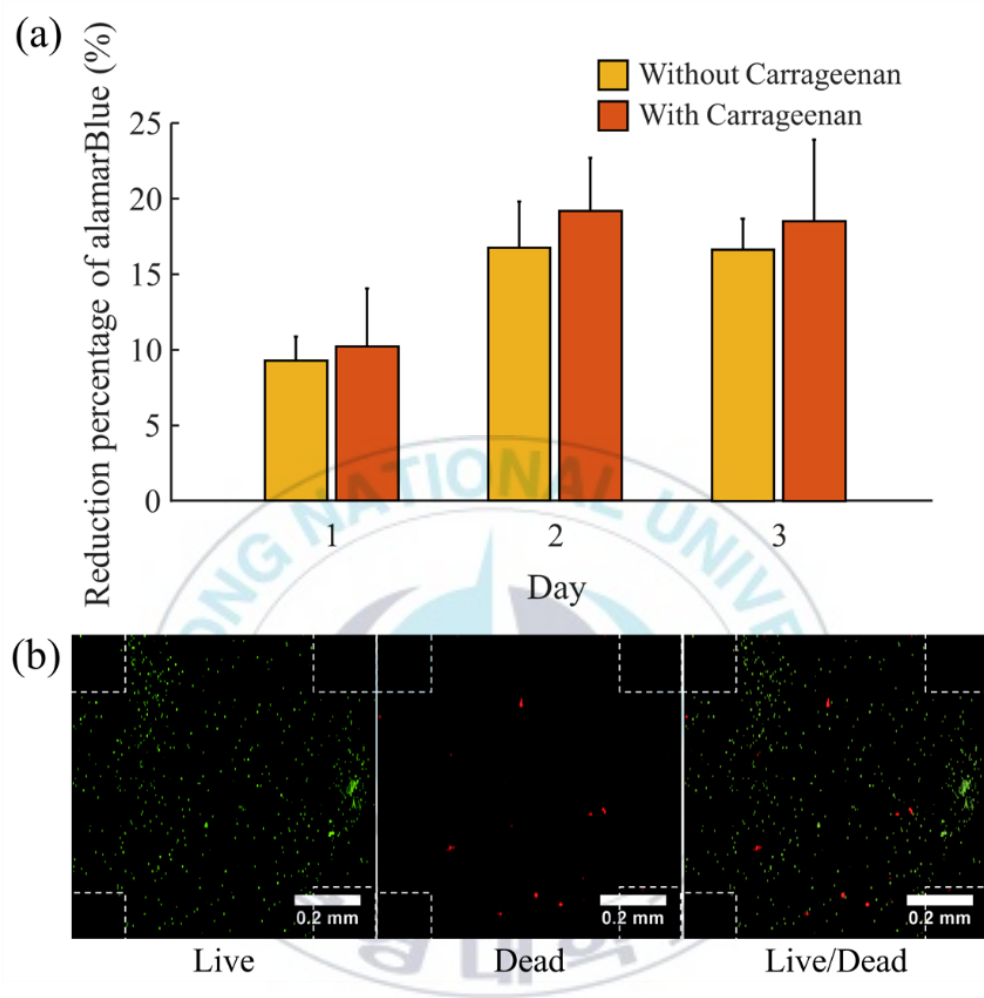


Figure 19. Biological activities of 3D-bioprinted scaffolds: (a) Cell proliferation with alamarBlue reagent in Alg-CaSO₄ and Alg-Carr-CaSO₄ scaffolds; (b) Confocal fluorescence images of live (green) and dead (red) cells in 3D-bioprinted scaffolds using Alg-Carr-CaSO₄ composite hydrogels after 24 hours.

3.3. Discussion

In this study, based on the simulation and measurement of rheological properties of Alg-CaSO₄ and Alg-Carr-CaSO₄, optimum printing parameters were explored for fabricating superior scaffolds with enhanced printability. We also demonstrated the effects of Carr on the rheological and thixotropic properties of the alginate-based hydrogel. Therefore, the 3D-printed structure made of Alg-Carr-CaSO₄ had better shape fidelity than Alg-CaSO₄ after the 3D deposition of multiple layers. Eventually, the live/dead assay proved that Alg-Carr-CaSO₄ is biocompatible and can be used as a biomaterial for extrusion-based bioprinting for tissue engineering applications.

Recently, numerous biomaterials have been developed for applying in tissue engineering and regenerative medicine. However, without considering the rheological properties of the biomaterials, it is difficult to determine the optimum printing parameters for extrusion-based bioprinting [22]. The printing parameters for bioprinting differ depending on the rheological properties of the biomaterial in use, e.g. shear thinning, thixotropic behavior or viscoelasticity [36]. Thus, the assessment of rheological properties needs to be considered for the development of bioink as well as the optimization of 3D bioprinting. A number of results have been reported evaluating the printability of biomaterials using rheological studies [37, 38]. Determining the appropriate printing parameters through printability evaluation based on the rheological study would enhance both stability and speed of bioprinting. It has been known that the increase of the viscosity of the biomaterial improves the fidelity of the printed structure

[39]. However, when a biomaterial having high mechanical strength and viscosity encapsulate with cells, high shear stress can act as a negative influence on suspended cells in the biomaterials as well as not be fully distributed [40]. In this study, as shown in Figure 19, optimized printing parameters that do not significantly affect the viability of evenly suspended cells can easily be determined by printability evaluation based on the rheological assessment of biomaterials.

An alginate chain is composed of β -D-mannuronic acid (M) and α -L-guluronic acid (G), arranged in a random sequence of M and G blocks interspersed with regions of alternating MG blocks. The G blocks provide ionic crosslinking with calcium ions by forming egg-box model that contribute to the increased mechanical strength of the Alg [41]. Since the concentration of Alg affects the rheological and mechanical properties of the material and also the crosslinking time with the crosslinking agent, we fixed the final concentration of Alg to 2% [42]. The Alg concentrations of 2-4% have been found to be chemically, biologically and mechanically stable especially used in extrusion-based bioprinting [10]. As shown in Figure 10(b), the storage modulus of Alg crosslinked with CaSO_4 tends to decrease if the CaSO_4 concentration is more than 1%. The exceeded concentration of calcium ions most likely affects the mechanical strength of the solution leading to decreased storage modulus. The Alg has a carboxyl group while Carr has a sulfate and carboxyl group, which results in gelation through ionic crosslinking with the divalent cation of calcium ions [43]. Thus, as shown in Figure 10, 11, 12, and 13, using calcium sulfate, Carr clearly increased the maximum mechanical strength and rheological properties of Alg- CaSO_4 .

The printability simulation of the printed strut diameter concerning the flow rate and the printing speed can be very useful for improving the printability of the actual 3D bioprinting [44]. However, there is a possibility of the differences between the simulated and actual printing results for shear-thinning hydrogels due to the simplified conditions in the derived equations, e.g., the compressibility of the materials, slip on the wall of the syringe, die swell effect possibly occurring at the nozzle end, and the change in recovery behavior of materials after inflicting high shear rate [32]. In reality, although the nozzle size of 0.51 mm was used, the proper diameters of the printed struts were approximately 0.7-0.8 mm, which were located at the slightly right side of the ideal printability (0 in log scale) presented in Figure 14, 15, 16 and 17. This might result from the effects of shear forces such as gravity leading deformation of the structure, surface tension, dehydration, and intrinsic heterogeneity of the biomaterials [45]. Also, in addition to the printability simulation based on the power law model, simulation with more complicated models needs to be considered for various bioinks with non-Newtonian properties.

This study aimed to improve the printability of hydrogels and mechanical properties of materials to make them suitable for bioink in tissue engineering and regenerative medicine. The Alg-Carr-CaSO₄ presented in this thesis is a promising biomaterial for extrusion-based bioprinting. We showed the suitability of Alg-Carr-CaSO₄ through simulation and 3D printing. In the future, the biological interactions and biodegradability in the physiological conditions of 3D-printed Alg-Carr-CaSO₄

composite scaffold through the *in vitro* study followed by the *in vivo* study needs to be considered.



3.4. Conclusion

This study presented a novel bioink composed of Alg and Carr for the extrusion-based bioprinting. The rheological properties of alginate-based hydrogel improved as the concentration of Carr in the composite hydrogels increased and was best when the Carr concentration of 1.5% was used. We optimized printing parameters based on the rheological properties and applied them on Alg-CaSO₄ and Alg-Carr-CaSO₄ composites. As a result, we demonstrated excellent structural strength and printability of the Carr composite without significant negative effects on the cell viability. Finally, with the optimal printing conditions, the Alg-Carr-CaSO₄ has potential to become a prospective bioink for fabricating promising 3D-printed scaffold with remarkable mechanical properties while maintaining the structure and biological activity in the field of tissue engineering and regenerative medicine.

4. Conclusions

The investigation presented in this thesis could serve a methodological solution for improving the 3D printability and enhancing shape fidelity of the 3D-printed structure based on the physicochemical and rheological properties of biomaterials. With the optimal printing parameters concerning characteristics of injectable biomaterials, the well-constructed 3D structure could be directly fabricated for various applications in the field of tissue engineering and regenerative medicine using extrusion-based 3D bioprinting system within a short manufacturing time. The developed structure fabricated with optimized materials using bioprinting could provide an useful strategy for tissue regeneration in microenvironment.

5. References

- [1] Cohen, D. L., et al., Additive manufacturing for in situ repair of osteochondral defects, *Biofabrication*, 2 (2010) 035004.
- [2] Pati, F., et al., 3D bioprinting of tissue/organ models, *Angewandte Chemie International Edition*, 55 (2016) 4650-4665.
- [3] Dutta, R. C., Dutta, A. K., Cell-interactive 3D-scaffold; advances and applications, *Biotechnology advances*, 27 (2009) 334-339.
- [4] Lee, J.-H., et al., Fabrication and characterization of 3D scaffold using 3D plotting system, *Chinese science bulletin*, 55 (2010) 94-98.
- [5] Murphy, S. V., Atala, A., 3D bioprinting of tissues and organs, *Nature biotechnology*, 32 (2014) 773.
- [6] Ozbolat, I. T., Hospodiuk, M., Current advances and future perspectives in extrusion-based bioprinting, *Biomaterials*, 76 (2016) 321-343.
- [7] Jiang, T., et al., Extrusion bioprinting of soft materials: An emerging technique for biological model fabrication, *Applied Physics Reviews*, 6 (2019) 011310.
- [8] Kang, K., et al., Quantitative optimization of solid freeform deposition of aqueous hydrogels, *Biofabrication*, 5 (2013) 035001.
- [9] Ouyang, L., et al., Effect of bioink properties on printability and cell viability for 3D bioplotting of embryonic stem cells, *Biofabrication*, 8 (2016) 035020.
- [10] Hospodiuk, M., et al., The bioink: a comprehensive review on bioprintable materials, *Biotechnology advances*, 35 (2017) 217-239.
- [11] Zhao, Y., et al., The influence of printing parameters on cell survival rate and printability in microextrusion-based 3D cell printing technology, *Biofabrication*, 7 (2015) 045002.
- [12] Sachlos, E., Czernuszka, J., Making tissue engineering scaffolds work. Review: the application of solid freeform fabrication technology to the production of tissue engineering scaffolds, *Eur Cell Mater*, 5 (2003) 39-40.
- [13] Ishaug-Riley, S. L., et al., Human articular chondrocyte adhesion and proliferation on synthetic biodegradable polymer films, *Biomaterials*, 20 (1999) 2245-2256.
- [14] Baji, A., et al., Processing methodologies for polycaprolactone-hydroxyapatite composites: a review, *Materials and manufacturing processes*, 21 (2006) 211-218.
- [15] Marra, K. G., et al., In vitro analysis of biodegradable polymer blend/hydroxyapatite composites for bone tissue engineering, *Journal of Biomedical Materials Research: An Official Journal of The Society for Biomaterials, The Japanese Society for Biomaterials, and The Australian*

- Society for Biomaterials and the Korean Society for Biomaterials, 47 (1999) 324-335.
- [16] Chen, B., Sun, K., Poly (ϵ -caprolactone)/hydroxyapatite composites: effects of particle size, molecular weight distribution and irradiation on interfacial interaction and properties, *Polymer Testing*, 24 (2005) 64-70.
- [17] Chen, J.-P., Chang, Y.-S., Preparation and characterization of composite nanofibers of polycaprolactone and nanohydroxyapatite for osteogenic differentiation of mesenchymal stem cells, *Colloids and Surfaces B: Biointerfaces*, 86 (2011) 169-175.
- [18] Gasperini, L., et al., Natural polymers for the microencapsulation of cells, *Journal of the Royal Society Interface*, 11 (2014) 20140817.
- [19] Panwar, A., Tan, L., Current status of bioinks for micro-extrusion-based 3D bioprinting, *Molecules*, 21 (2016) 685.
- [20] Nakamura, M., et al., Biomatrices and biomaterials for future developments of bioprinting and biofabrication, *Biofabrication*, 2 (2010) 014110.
- [21] Kyle, S., et al., 'Printability' of Candidate Biomaterials for Extrusion Based 3D Printing: State-of-the-Art, *Advanced healthcare materials*, 6 (2017) 1700264.
- [22] Kesti, M., et al., Guidelines for standardization of bioprinting: A systematic study of process parameters and their effect on bioprinted structures, *BioNanoMaterials*, 17 (2016) 193-204.
- [23] Di Giuseppe, M., et al., Mechanical behaviour of alginate-gelatin hydrogels for 3D bioprinting, *Journal of the mechanical behavior of biomedical materials*, 79 (2018) 150-157.
- [24] Radhakrishnan, J., et al., Injectable and 3D bioprinted polysaccharide hydrogels: from cartilage to osteochondral tissue engineering, *Biomacromolecules*, 18 (2016) 1-26.
- [25] Markstedt, K., et al., 3D bioprinting human chondrocytes with nanocellulose–alginate bioink for cartilage tissue engineering applications, *Biomacromolecules*, 16 (2015) 1489-1496.
- [26] Yermak, I., Khotimchenko, Y. S., Chemical properties, biological activities and applications of carrageenan from red algae, *Recent advances in marine biotechnology*, 9 (2003) 207-255.
- [27] MacArtain, P., et al., Physical characteristics of calcium induced κ -carrageenan networks, *Carbohydrate Polymers*, 53 (2003) 395-400.
- [28] Liu, J., et al., Review for carrageenan-based pharmaceutical biomaterials: favourable physical features versus adverse biological effects, *Carbohydrate Polymers*, 121 (2015) 27-36.
- [29] Popa, E. G., et al., Seaweed polysaccharide-based hydrogels used for the regeneration of articular cartilage, *Critical Reviews in Biotechnology*, 35 (2015) 410-424.

- [30] Roh, Y. H., Shin, C. S., Preparation and characterization of alginate–carrageenan complex films, *Journal of applied polymer science*, 99 (2006) 3483-3490.
- [31] Mihaila, S. M., et al., Photocrosslinkable kappa-carrageenan hydrogels for tissue engineering applications, *Advanced healthcare materials*, 2 (2013) 895-907.
- [32] Suntornnond, R., et al., A mathematical model on the resolution of extrusion bioprinting for the development of new bioinks, *Materials*, 9 (2016) 756.
- [33] Malkin, A. Y., Isayev, A. I., *Rheology: concepts, methods, and applications*, Elsevier 2017.
- [34] Li, H., et al., Rheological study on 3D printability of alginate hydrogel and effect of graphene oxide, *Int. J. Bioprinting*, 2 (2016) 54-66.
- [35] Nam, S. Y., Park, S.-H., ECM Based Bioink for Tissue Mimetic 3D Bioprinting, *Biomimetic Medical Materials*, Springer 2018, pp. 335-353.
- [36] Das, S., et al., Bioprintable, cell-laden silk fibroin–gelatin hydrogel supporting multilineage differentiation of stem cells for fabrication of three-dimensional tissue constructs, *Acta biomaterialia*, 11 (2015) 233-246.
- [37] Müller, M., et al., Nanostructured Pluronic hydrogels as bioinks for 3D bioprinting, *Biofabrication*, 7 (2015) 035006.
- [38] Tirella, A., et al., A phase diagram for microfabrication of geometrically controlled hydrogel scaffolds, *Biofabrication*, 1 (2009) 045002.
- [39] Malda, J., et al., 25th anniversary article: engineering hydrogels for biofabrication, *Advanced materials*, 25 (2013) 5011-5028.
- [40] Billiet, T., et al., The 3D printing of gelatin methacrylamide cell-laden tissue-engineered constructs with high cell viability, *Biomaterials*, 35 (2014) 49-62.
- [41] Kong, H. J., et al., Independent control of rigidity and toughness of polymeric hydrogels, *Macromolecules*, 36 (2003) 4582-4588.
- [42] Ahn, S., et al., Cells (MC3T3-E1)-laden alginate scaffolds fabricated by a modified solid-freeform fabrication process supplemented with an aerosol spraying, *Biomacromolecules*, 13 (2012) 2997-3003.
- [43] Mammarella, E. J., Rubiolo, A. C., Crosslinking kinetics of cation-hydrocolloid gels, *Chemical Engineering Journal*, 94 (2003) 73-77.
- [44] Khalil, S., Sun, W., Biopolymer deposition for freeform fabrication of hydrogel tissue constructs, *Materials Science and Engineering: C*, 27 (2007) 469-478.
- [45] Xu, X., et al., Gravity and surface tension effects on the shape change of soft materials, *Langmuir*, 29 (2013) 8665-8674.

Acknowledgements

박사 유학을 가겠다는 꿈 하나로 시작한 융합재생의학연구실에서의 4 년간의 생활은 제 인생에 커다란 뿌리가 되었습니다. 어디에서도 못 해볼 풍부한 연구 및 실험 경험과 연구자로서의 소양을 얻을 수 있어 앞으로의 박사 생활에 많은 도움이 될 것 같습니다. 자유로운 연구실 분위기에서 제가 하고 싶은 연구들에 대해 많은 조언과 아낌없는 지원을 해주신 남승운 지도교수님께 감사의 마음을 전합니다. 바쁘신 와중에도 저의 논문 심사를 해주시고 항상 저에게 따뜻한 격려와 조언을 해주신 정원교 교수님과 박상혁 교수님께 감사의 말씀을 드립니다. 또, 부족하지 않은 연구 결과를 위해 많은 연구 장비를 이용하게 해주신 오정환 교수님과 방대한 전공지식뿐만 아니라 올바른 마음가짐에 대해 항상 알려주시던 이명기 교수님, 안예찬 교수님, 강현욱 교수님께 감사 드립니다.

많은 시행착오를 함께 겪고 이겨낸 연구실 첫 멤버인 윤철희 선배님, 유진명 선배님, 최보영 후배님과 유학생들의 고됨을 누구보다 잘 알고 많은 조언을 해준 Elna Paul Chalisserry, 다른 곳에서 서로의 길을 열심히 응원해주고 달려나가고 있는 석지민, 연구를 하면서 많은 도움을 준 동료 연구원들께 감사의 말씀을 전하고 싶습니다. 그리고 힘든 배움의 시간 속에서 많은 의지가 되어준 학과 동기들과 선배님들, 후배님들께 감사 드립니다.

마지막으로 언제나 저를 응원해주시고 밀어주시는 사랑하는 부모님과 누나에게 진심으로 감사 드립니다.

석사학위까지의 뜻 깊은 생활과 감사한 마음들을 가지고 미국에서의 성공적인 박사생활과 저의 꿈을 위해 열심히 달려나가겠습니다. 감사합니다.